Inorganic Chemistry

pubs.acs.org/IC Featured Article

Ag(III)···Ag(III) Argentophilic Interaction in a Cofacial Corrole Dyad

Christopher M. Lemon,* David C. Powers, Michael Huynh, Andrew G. Maher, Austin A. Phillips, Brian P. Tripet, and Daniel G. Nocera*



Cite This: Inorg. Chem. 2023, 62, 3-17



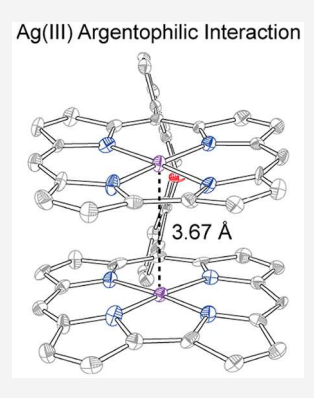
ACCESS I

III Metrics & More

Article Recommendations

SI Supporting Information

ABSTRACT: Metallophilic interactions between closed-shell metal centers are exemplified by d¹⁰ ions, with Au(I) aurophilic interactions as the archetype. Such an interaction extends to d⁸ species, and examples involving Au(III) are prevalent. Conversely, Ag(III) argentophilic interactions are uncommon. Here, we identify argentophilic interactions in silver corroles, which are authentic Ag(III) species. The crystal structure of a monomeric silver corrole is a dimer in the solid state, and the macrocycle exhibits an atypical domed conformation. In order to evaluate whether this represents an authentic metallophilic interaction or a crystal-packing artifact, the analogous cofacial or "pacman" corrole was prepared. The conformation of the monomer was recapitulated in the silver pacman corrole, exhibiting a short 3.67 Å distance between metal centers and a significant compression of the xanthene backbone. Theoretical calculations support the presence of a rare Ag(III)···Ag(III) argentophilic interaction in the pacman complex.



INTRODUCTION

Bonding between metal centers can be categorized into three regimes: metallic, covalent, and metallophilic. Of these, the less common metallophilic (dispersion) interaction forms between closed-shell metal ions and does not involve the pairing of electrons, as observed in the formation of a distinct metal—metal bond. Energy stabilization through metallophilic interactions can be rationalized with the molecular orbital diagram shown in Figure 1, adapted from Doerrer. A filled d orbital, either $d_{x^2-y^2}$ for d^{10} ions or d_z^2 for d^{8} ions, overlaps with an identical orbital on an adjacent metal center, giving rise to filled bonding (FF) and antibonding (FF*) combinations. Unfilled p orbitals can similarly produce empty bonding (EE) and antibonding (EE*) combinations. If the unfilled orbitals

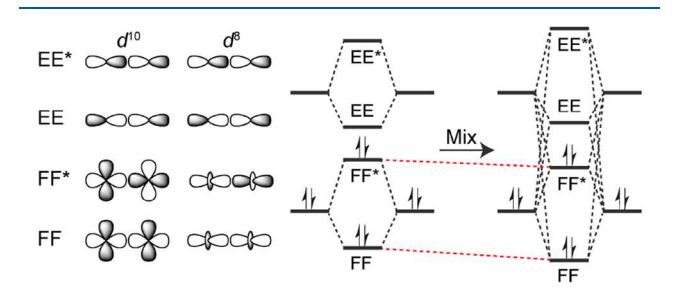


Figure 1. Illustration of the bonding and antibonding orbital interactions between filled d orbitals (FF and FF*) and empty p orbitals (EE and EE*) with the corresponding molecular orbital diagram. If the empty orbitals are low enough in energy and have the proper symmetry, they mix with the filled orbitals, lowering the energy of the FF and FF* orbitals to result in an overall stabilization of the metallophilic interaction relative to two noninteracting metal centers.

are sufficiently low in energy and have the same symmetry as the filled orbitals, then the filled and unfilled orbitals can mix. This mixing lowers the energy of the FF and FF* orbitals, resulting in a net stabilization of the metallophilic pair relative to the individual metal centers.

The energy of metallophilic interactions is on the order of hydrogen bonds,³ which can have a significant influence on the ground-state geometry of a molecule or dyad. As a result, metallophilicity is often identified by X-ray crystallography, where the distance between metal centers is shorter than the sum of the van der Waals radii. Metallophilicty between Au centers, also known as aurophilic interactions, 4,5 is most readily observed for Au(I) complexes, where the Au···Au contacts are less than 3.32 Å.6 Recent reports of Au(I)···Au(I) aurophilic interactions exhibit distances of 2.9579 and 2.9529 Å. While metallophilic interactions are most common between d10 centers, this phenomenon also prevails for d8 [e.g., Au(III) and Pt(II)] and s² [e.g., Pb(II) and Bi(III)] configurations. 1,2,8,9 An early example of a d8...d8 metallophilic interaction is the binuclear μ -diphosphitoplatinum(II) complex $[Pt_2(P_2O_5H_2)_4]^{4-}, \ also \ known \ as \ Pt(pop).^{10,11} \ The \ initial$ crystal structure revealed a 2.925 Å distance between Pt centers, 12 and the Pt...Pt interaction was characterized by resonance Raman spectroscopy. 13 The first examples of d8...d8

Received: June 30, 2022 Published: December 20, 2022

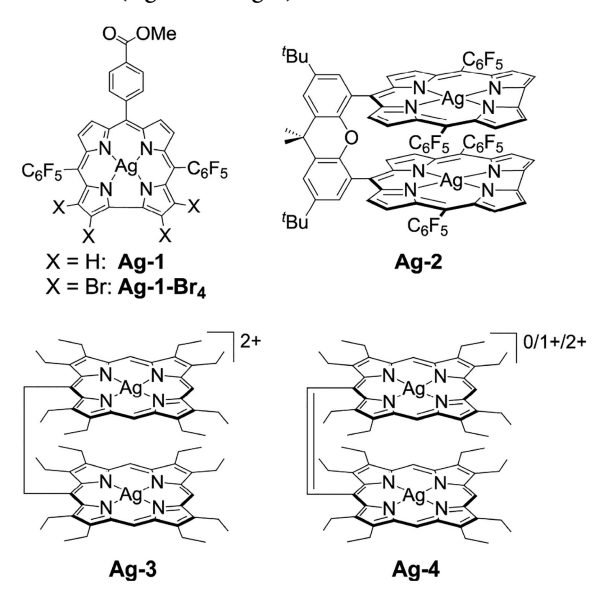




Au(III) aurophilic interactions were observed in [Me₄N][Au-(N₃)₄]¹⁴ and [Au(bpy)Cl₂][AuBr₄], ¹⁵ which exhibit Au···Au distances of 3.507 and 3.518 Å, respectively, values that are larger than the sum of the van der Waals radii of two Au atoms (3.32 Å). ⁶ These experimental observations are consistent with early computational results, which predicted that the M···M distance in metallophilic interactions increases with increasing oxidation state. ¹⁶

While argentophilic interactions are pervasive for Ag(I) centers, 17 they have only recently been identified for Ag(III) species. The rarity of Ag(III) complexes has hampered the observation of such interactions. 18,19 Double oxidation of a Ag(II) porphyrin dimer with a flexible ethane linker ($-CH_2-CH_2-$) furnishes the Ag(III) dimer (Chart 1), which exhibits a

Chart 1. Corroles Examined in This Study and Other Reported Examples of Ag(III)···Ag(III) Argentophilic Interactions (Ag-3 and Ag-4)



short Ag...Ag distance of 3.659 Å in the solid state for the $[SbF_6]^-$ salt or 3.463 Å for the $[PF_6]^-$ salt. At 77 K, this complex exhibits an emission feature at 546 nm, suggestive of a metallophilic interaction. This is further supported by theoretical calculations and represents the first example of a Ag(III)···Ag(III) argentophilic interaction. A similar study was conducted using ethene-bridged Ag(II) porphyrin dimers (Chart 1). Stepwise oxidation resulted in shorter Ag...Ag distances: 3.61 Å for Ag(II)/Ag(II), 3.53 Å for mixed-valent Ag(II)/Ag(III), and 3.45 Å for Ag(III)/Ag(III). A Bader analysis revealed that the strength of the Ag...Ag interaction increases with the oxidation state.²¹ Because β -unsubstituted silver corroles are authentic Ag(III) species, ^{22–27} rather than Ag(II) complexes with a noninnocent ligand [i.e., a Ag(II) corrole radical cation], as in the case of copper corroles, silver corroles offer an ideal platform to observe Ag(III)··· Ag(III) argentophilic interactions.

Here, we explore the electronic structure of silver corrole complexes (Chart 1) using a variety of characterization techniques and draw comparisons to $[TBA][Ag(CF_3)_4]$ as an authentic Ag(III) complex. Consistent with previous results, silver corroles are best formulated as Ag(III) complexes. A monomeric silver corrole (Ag-1) exhibits a cofacial arrangement of two corrole units in the solid state. A unique domed

conformation of the ligand enables close contact between Ag centers (3.75 Å). To determine if this dimeric structure is a consequence of an authentic metal—metal interaction or simply a crystal packing effect, the analogous cofacial corrole dyad or "pacman" derivative was prepared.³² The silver pacman Ag-2 exhibits the same structural features as the monomer with a shorter Ag···Ag distance of 3.67 Å. Theoretical calculations, including Bader and natural bond order (NBO) analyses, confirm the presence of a weak, closed-shell dispersion interaction between Ag centers, providing a rare example of a Ag(III)···Ag(III) argentophilic interaction.

■ EXPERIMENTAL SECTION

Materials. The following materials were used as received: hexane, dichloromethane (CH₂Cl₂), chloroform (CHCl₃), pyridine, tetrahydrofuran (THF), N,N-dimethylformamide (DMF), trifluoroacetic acid (TFA), 2,3-dichloro-5,6-dicyano-1,4-benzoquinone (DDQ), nbutyllithium 2.5 M solution in hexanes (nBuLi), 4,5-dibromo-2,7-ditert-butyl-9,9-dimethylxanthene, gold foil, spray-dried potassium fluoride (KF), silver(I) fluoride (AgF), silver(II) fluoride (AgF2), tetrabutylammonium bromide (TBABr), trimethyl(trifluoromethyl)silane (TMSCF₃), and silica gel (60 Å pore size, 230-400 mesh or 40-63 μ m particle size), from Sigma-Aldrich; silver(I) acetate [Ag(OAc)] from Strem; sodium sulfate (Na₂SO₄) from Mallinckrodt; gold(III) acetate [Au(OAc)₃] from Alfa Aesar; chloroform-d (CDCl₃) and toluene-d₈ from Cambridge Isotope Laboratories. Argon gas (Airgas) was passed over a Drierite column prior to use. Tetrabutylammonium hexafluorophosphate ([TBA][PF₆]) from Sigma-Aldrich was recrystallized from ethanol and subsequently dried under vacuum prior to use. The acetonitrile (MeCN) used for electrochemical experiments was purchased from Sigma-Aldrich, dispensed from a solvent drying system (Pure Process Technologies), and stored over 3 Å molecular sieves. Pentafluorophenyldipyrromethane, 10-(4-methoxycarbonylphenyl)-5,15-bis-(pentafluorophenyl)corrole (1) and 2,3,17,18-tetrabromo-10-(4methoxycarbonylphenyl)-5,15-bis(pentafluorophenyl)corrole (1-Br₄) were prepared according to literature methods.3

10-(4-Methoxycarbonylphenyl)-5,15-bis-(pentafluorophenyl)corrolotosilver(III) (Ag-1). In a roundbottom flask, 97 mg of the free-base corrole 1 (0.13 mmol) was dissolved in 13 mL of pyridine, and 132 mg of Ag(OAc) (0.791 mmol) was added. The resultant green solution was heated to 80 °C, 258 mg of Ag(OAc) (1.54 mmol) was added, and the reaction was allowed to continue for 2 h to afford a red solution. Solvent was removed by rotary evaporation. The crude reaction mixture was purified on a silica gel column packed with hexanes. The product eluted as a red band using a 1:1 mixture of hexanes and CH₂Cl₂. Solvent was removed by rotary evaporation to afford 72 mg (63% yield) of the title product as a red solid. ¹H NMR (500 MHz, CDCl₃, 23 °C): δ 4.12 (s, 3H), 8.31 (d, J = 8.1 Hz, 2H), 8.48 (d, J = 8.1 Hz, 2H), 8.78 (d, J = 4.5 Hz, 2H), 8.87 (d, J = 4.9 Hz, 2H), 8.92 (d, J = 4.7 Hz, 2H), 9.36 (d, J = 4.4 Hz, 2H). ¹⁹F NMR (470 MHz, CDCl₃, 25 °C): δ –162.99 (m, 4F), –153.87 (t, J = 20.9 Hz, 2F), –138.57 $(dd, J^1 = 24.9 \text{ Hz}, J^2 = 7.8 \text{ Hz}, 4\text{F})$. Anal. Calcd for M⁺, where M = C₃₉H₁₅AgF₁₀N₄O₂: 868.01. Found by LD-MS: 868.09. UV-vis [toluene; λ , nm (ε , ×10³ M⁻¹ cm⁻¹)]: 406 (38), 427 (116), 499 (3.7), 536 (7.6), 574 (31).

2,3,17,18-Tetrabromo-10-(4-methoxycarbonylphenyl)-5,15-bis(pentafluorophenyl)corrolotosilver(III) (Ag-1-Br₄). In a 20 mL scintillation vial, 58 mg of the free-base corrole **1-Br₄** (54 μ mol) was dissolved in 5 mL of pyridine, and 208 mg of Ag(OAc) (1.2 mmol) was added. The resultant mixture was heated at 80 °C, an additional 230 mg of Ag(OAc) (1.4 mmol) was added, and the reaction was allowed to continue for 1 h to afford a red solution. The crude reaction mixture was filtered over a plug of silica gel, eluting with CH₂Cl₂. After solvent removal, the residue was purified on a silica gel column using a 1:1 mixture of hexanes and CH₂Cl₂. Solvent was removed by rotary evaporation to afford 31 mg (49% yield) of the

title product as a red solid. 1 H NMR (500 MHz, CDCl₃, 25 $^{\circ}$ C): δ 4.11 (s, 3H), 8.24 (d, J = 8.1 Hz, 2H), 8.48 (d, J = 8.1 Hz, 2H), 8.71 (d, J = 4.9 Hz, 2H), 8.74 (d, J = 4.9 Hz, 2H). 19 F NMR (470 MHz, CDCl₃, 25 $^{\circ}$ C): δ -163.29 (m, 4F), -152.83 (t, J = 20.9 Hz, 2F), -138.88 (m, 4F). Anal. Calcd for M⁺, where M = C₃₉H₁₁AgBr₄F₁₀N₄O₂: 1183.65. Found by LD-MS: 1183.63. UV-vis [toluene; λ , nm (ε , ×10³ M⁻¹ cm⁻¹)]: 407 (55), 428 (131), 504 (4.5), 538 (12), 580 (72).

4,5-Diformyl-2,7-di-tert-butyl-9,9-dimethylxanthene (4). In a 250 mL oven-dried Schlenk flask, 100 mL of dry THF was dispensed from a solvent drying station under argon. Then 2.01 g of 4,5-dibromo-2,7-di-tert-butyl-9,9-dimethylxanthene (4.2 mmol) was added under a flow of argon. The resultant solution was cooled to −78 °C in a dry ice/acetone bath, then 7 mL of nBuLi (17.5 mmol) was added, and the resultant mixture was stirred at -78 °C for 1 h. Then 8 mL of DMF (7.6 g, 103 mmol) was added. The reaction mixture was slowly warmed to room temperature and stirred for an additional 1 h. Water was added (~100 mL), and the product was extracted with CH₂Cl₂ (×3). The combined organics were washed with water (×2) and brine, dried over Na₂SO₄, and brought to dryness. The residue was purified on a silica gel column using CHCl₃ as the eluent. Solvent was removed to afford 1.54 g (97% yield) of the title product as a white solid. ¹H NMR (500 MHz, CDCl₃, 25 °C): δ 1.37 (s, 18H), 1.70 (s, 6H), 7.71 (d, J = 2.5 Hz, 2H), 7.82 (d, J = 2.5Hz, 2H), 10.68 (s, 2H). Anal. Calcd for $(M + H)^+$, where M = $C_{25}H_{32}O_3$: 379.22. Found by LD-MS: 379.11. UV-vis (CH₂Cl₂; λ , nm): 256, 333.

Synthesis of the Pacman Corrole. In a 500 mL oven-dried Schlenk flask, 300 mL of dry CH₂Cl₂ was dispensed from a solvent drying station under argon. Then 509 mg of 4 (1.3 mmol) and 2.92 g of pentafluorophenyldipyrromethane (9.4 mmol) were added under a flow of argon, followed by 150 μ L (2 mmol) of TFA. The resultant solution was stirred at room temperature for 4 h protected from light. The reaction mixture was poured into a 2 L round-bottom flask containing 1.5 L of CH₂Cl₂, and 1.85 g of DDQ (8.1 mmol) was added. The solution immediately turned dark, and the solution was stirred for 15 min. The reaction mixture was concentrated to near dryness and then poured onto a silica gel column; all of the fluorescent material was eluted with CH2Cl2. After removal of the solvent, the residue was purified on a silica gel column using CH₂Cl₂ as the sole eluent. Two fluorescent products were observed. The first fraction was identified as the pacman corrole 2, which eluted as a dark violet solution; the product was isolated as a dark purple solid in 26% yield (553 mg). The second fraction was identified as the monomeric corrole 5, which also eluted as a violet solution; the product was obtained as a dark purple solid in 23% yield (304 mg).

4,5-Bis[5,15-bis(pentafluorophenyl)corrol-10-yl]-2,7-di-tert-butyl-9,9-dimethylxanthene (2). 1 H NMR (500 MHz, CDCl₃, 25 $^\circ$ C): δ 1.37 (s, 18H), 2.21 (s, 6H), 7.33 (d, J = 2.4 Hz, 2H), 7.88 (d, J = 2.4 Hz, 2H), 7.90 (d, J = 4.2 Hz, 4H), 8.00 (d, J = 4.7 Hz, 4H), 8.06 (bs, 4H), 8.47 (d, J = 4.2 Hz, 4H). 19 F NMR (470 MHz, CDCl₃, 25 $^\circ$ C): δ -164.20 (m, 4F), -162.03 (m, 4F), -153.75 (t, J = 20.6 Hz, 4F), -138.26 (m, 4F), -136.45 (bs, 4F). Anal. Calcd for M $^+$, where M = C₈₅H₅₂F₂₀N₈O: 1578.38. Found by LD-MS: 1578.38. UV-vis (CH₂Cl₂; λ , nm): 262, 293, 401, 522, 567, 624.

4-[5,15-Bis(pentafluorophenyl)corrol-10-yl]-5-formyl-2,7-di-tertbutyl-9,9-dimethylxanthene (5). 1 H NMR (500 MHz, CDCl₃, 25 $^{\circ}$ C): δ 1.26 (s, 9H), 1.53 (s, 9H), 1.93 (s, 6H), 7.38 (d, J = 2.4 Hz, 1H), 7.74 (d, J = 2.4 Hz, 1H), 7.86 (s, 1H), 7.88 (d, J = 2.4 Hz, 1H), 7.99 (d, J = 2.4 Hz, 1H), 8.56 (bs, 2H), 8.65 (m, 4H), 9.13 (d, J = 4.2 Hz, 2H). 19 F NMR (470 MHz, CDCl₃, 25 $^{\circ}$ C): δ −163.45 (bs, 2F), −163.00 (bs, 2F), −154.40 (bs, 2F), −139.35 (bm, 2F), −138.45 (bm, 2F). Anal. Calcd for (M + H) $^{+}$, where M = C₅₅H₄₂F₁₀N₄O₂: 979.30. Found by LD-MS: 979.34. UV-vis (CH₂Cl₂; λ , nm): 263, 412, 426, 521, 563, 613, 640.

4,5-Bis[5,15-bis(pentafluorophenyl)corrol-10-ylsilver]-2,7-di-*tert*-butyl-9,9-dimethylxanthene (Ag-2). In a 20 mL scintillation vial, 65 mg of free-base corrole 2 (41 μ mol) was dissolved in 5 mL of pyridine, and 236 mg of Ag(OAc) (1.41 mmol) was added. The resultant mixture was stirred at 80 °C for 1.5 h. The crude

reaction mixture was filtered over a plug of silica using CH₂Cl₂ as the eluent. After solvent removal, the residue was purified on a silica gel column with CH₂Cl₂ and the product eluted as a red solution, giving 67 mg (91% yield) of the title compound as a red solid. ¹H NMR (500 MHz, CDCl₃, 25 °C): δ 1.40 (s, 18H), 2.23 (s, 6H), 7.39 (d, J = 2.4 Hz, 2H), 7.89 (d, J = 2.4 Hz, 2H), 8.16 (bd, J = 4.2 Hz, 4H), 8.18 (d, J = 4.7 Hz, 4H), 8.20 (bd, J = 4.8 Hz, 4H), 8.73 (d, J = 4.3 Hz, 4H). ¹⁹F NMR (470 MHz, CDCl₃, 25 °C): δ -165.45 (m, 4F), -163.41 (m, 4F), -155.03 (t, J = 20.8 Hz, 4F), -138.76 (dd, J¹ = 24.2 Hz, J² = 6.4 Hz, 4F), -136.57 (d, J = 23.9 Hz, 4F). Anal. Calcd for M⁺, where M = C₈₅H₄₆Ag₂F₂₀N₈O: 1788.14. Found by LD-MS: 1788.79. UV-vis (toluene; λ , nm): 411, 423, 502, 539, 576.

Gold Metalation of the Pacman Corrole 2. In a 10 mL microwave tube, 84 mg of 2 (53 μ mol) was dissolved in 5 mL of pyridine, and 315 mg of Au(OAc)₃ (0.84 mmol) was added. The resultant mixture was stirred at room temperature overnight. The crude reaction mixture was filtered over a plug of silica using CH₂Cl₂ as the eluent to give 9 mg of material as a red solid. Chromatography of the residue on silica gel using a 1:1 mixture of hexane and CH₂Cl₂ resolves two bands: an initial red band of the gold pacman complex (Au-2), followed by a green band of octaphyrin 6.

4,5-Bis[5,15-bis(pentafluorophenyl)corrol-10-ylgold]-2,7-di-tert-butyl-9,9-dimethylxanthene (**Au-2**). ¹H NMR (500 MHz, CDCl₃, 25 °C): δ 1.38 (s, 18H), 2.21 (s, 6H), 7.37 (d, J = 2.4 Hz, 2H), 7.87 (d, J = 2.4 Hz, 2H), 8.19 (d, J = 4.8 Hz, 4H), 8.21 (bd, J = 4.7 Hz, 4H), 8.25 (bd, J = 4.2 Hz, 4H), 8.74 (d, J = 4.5 Hz, 4H). ¹⁹F NMR (470 MHz, CDCl₃, 25 °C): δ -164.17 (m, 4F), -162.04 (m, 4F), -153.67 (t, J = 20.5 Hz, 4F), -137.34 (m, 4F), -134.99 (m, 4F). Anal. Calcd for M⁺, where M = $C_{85}H_{46}Au_2F_{20}N_8O$: 1966.27. Found by LD-MS: 1966.62. UV-vis (toluene; λ , nm): 324, 406, 416, 534, 570.

[34]Octaphyrin(1.1.1.0.1.1.1.0) (6). 1 H NMR (500 MHz, CDCl₃, 25 $^{\circ}$ C): δ 1.39 (s, 18H), 1.43 (s, 6H), 6.09 (bs, 2H), 6.38 (bs, 2H), 6.45 (bd, $J \sim 2.8$ Hz, 2H), 6.48 (bs, 2H), 6.59 (bs, 2H), 6.91 (bs, 2H), 7.31 (bs, 2H), 7.42 (bs, 2H), 7.69 (bs, 2H), 7.78 (bs, 2H), 12.98 (bs, 4H). 19 F NMR (470 MHz, CDCl₃, 25 $^{\circ}$ C): δ –165.04 (bm, 2F), –163.28 (bm, 2F), –161.35 (bm, 2F), –160.99 (bm, 2F), –153.08 (bm, 2F), –152.93 (bm, 2F), –137.84 (bm, 2F), –137.20 (bm, 2F), –131.99 (bm, 2F), –131.63 (bm, 2F). Anal. Calcd for (M + H)⁺, where M = $C_{85}H_{48}F_{20}N_8$ O: 1577.37. Found by LD-MS: 1577.48. UV-vis (CH₂Cl₂; λ , nm): 263, 313, 416, 506, 714, 772, 926, 1052.

Tetrabutylammonium Tetrakis(trifluoromethyl)argentate ([TBA][Ag(CF₃)₄]). In a 20 mL scintillation vial, 97 mg of AgF (0.76 mmol), 424 mg of spray-dried KF (7.3 mmol), 0.5 mL of DMF, and 1.6 mL of TMSCF₃ (1.57 g, 8.5 mmol) were stirred at room temperature for 30 min. An additional 0.6 mL of TMSCF₃ (0.59 g, 3.2 mmol) was added, and the slurry was stirred for an additional 4 h. After this time, 5 mL of water was added to the reaction mixture, followed by 259 mg of TBABr (0.80 mmol). An additional 10 mL of water was added to produce a sufficiently large aqueous layer, and the reaction mixture was extracted with CH₂Cl₂ (five times). The combined organics were dried over Na₂SO₄ and subsequently brought to dryness. The residue was dissolved in a minimal amount of CH₂Cl₂, and the reaction mixture was filtered over a plug of silica gel, eluting with CH2Cl2. The filtrate was brought to dryness, the residue was dissolved in 20 mL of diethyl ether, and 100 mL of hexanes was added to precipitate the product. The solid was collected on a frit and dried under vacuum overnight to afford 75 mg (16% yield) of the title product as a white solid. ¹H NMR (500 MHz, CDCl₃, 23 °C): δ 1.03 (t, J = 7.4 Hz, 12H), 1.43 (sextet, J = 7.5 Hz, 8H), 1.60 (m, 8H), 3.08(m, 8H). 19 F NMR (470 MHz, CDCl₃, 25 °C): δ –31.25 [dd, $^{2}J(^{107}Ag) = 35.6 \text{ Hz}, ^{2}J(^{109}Ag) = 40.7 \text{ Hz}, 12\text{F}]. \text{ Anal. Calcd for M}^{-},$ where $M = C_4AgF_{12}$: 382.8859. Found by ESI-MS: 382.8868. UV-vis (CH₂Cl₂; λ, nm): 245.

Physical Measurements. NMR spectra were recorded on a Varian Inova-500 NMR spectrometer at the Harvard University Department of Chemistry and Chemical Biology Laukien-Purcell Instrumentation Center. 1 H NMR spectra were internally referenced to the residual solvent signal ($\delta = 7.26$ for CHCl₃ in CDCl₃), 34 while 19 F NMR spectra were externally referenced to α, α, α -trifluorotoluene ($\delta = -63.72$). 1 H/ 109 Ag heteronuclear multiple quantum coherence

(HMQC) NMR spectra were recorded on a Bruker 400 MHz Ascend Avance NEO spectrometer at the Montana State University (MSU) Department of Chemistry and Biochemistry NMR Center. The ¹⁰⁹Ag chemical shift was externally referenced to a saturated solution of AgNO₃ ($\delta = -59.0$). Mass spectrometry (MS) spectra were recorded on a Bruker Autoflex MALDI-TOF mass spectrometer in positive-ion mode or an Agilent 6538 Q-TOF mass spectrometer in negative-ion mode at the Proteomics, Metabolomics, and Mass Spectrometry Facility at MSU. Absorption spectra were acquired using a Cary 5000 spectrometer (Agilent) or a Shimadzu UV-3101PC spectrometer. Emission spectra were recorded on a Photon Technology International QM4 fluorometer equipped with a 150 W Xe arc lamp and a Hamamatsu R2658 photomultiplier tube. Electrochemical measurements were made in a glovebox under a nitrogen atmosphere using a CH Instruments 760D Electrochemical Workstation with CHI version 10.03 software. Samples were prepared at concentrations of ~1 mM of the compound with 0.1 M [TBA][PF₆] as the supporting electrolyte in MeCN. Cyclic voltammograms (CVs) were recorded at a scan rate of 100 mV s⁻¹ using a glassy carbon button working electrode, a Ag wire reference electrode (isolated by a ceramic frit), and a Pt wire counter electrode. The CVs were internally referenced to ferrocene.

X-ray photoelectron spectroscopy (XPS) data were recorded using a Thermo Scientific K-Alpha XPS system. All samples were irradiated using a monochromated Al K α X-ray source (1486.6 eV energy and 0.85 eV line width) with a 400 μ m spot size. ³⁶ Surface charging was compensated for by a low-energy (0–14 eV) electron flood gun. The system was precalibrated with Au, Ag, and Cu standards built into the sample stage using an automated routine. Solutions of the sample were dropcast onto gold foil. Survey spectra were collected from 0 to 1350 eV with a step size of 1.0 eV. High-resolution spectra for the Ag 3d and C 1s regions were measured with a step size of 0.1 eV. Samples were calibrated to the C 1s peak at 284.8 eV.³⁷

Computational Details. Density functional theory (DFT) calculations were performed with the hybrid functional Becke-3 parameter exchange functional ^{38–40} and the Lee–Yang–Parr nonlocal correlation functional (B3LYP),⁴¹ as implemented in the Gaussian 09, revision D.01, software package. 42 To account for dispersion interactions, the ω B97X-D functional was utilized, ⁴³ as implemented in the Gaussian 16, revision A.03, software package. 44 For light atoms (H, C, N, O, and F), a polarized split-valence triple- ζ basis set that includes p functions on H atoms and d functions on other atoms [i.e., the 6-311G(d,p) or 6-311G** basis set] was used. 45,46 A Wood-Boring⁴⁷ quasi-relativistic effective core potential was used for Ag and Br (i.e., MWB28). All calculations were performed with a polarizable continuum (PCM) solvation model in toluene using a polarizable conductor calculation model (CPCM). 48,49 All optimized geometries were confirmed as local minima structures by calculating the Hessian matrix and ensuring that no imaginary eigenvalues were present. Calculated structures were rendered using the program Avogadro. Bader analyses 51,52 were performed using the program AIMAII.53 Wiberg bond orders⁵⁴ were determined by NBO analysis^{55,56} using NBO, version 3,⁵⁷ as implemented in Gaussian 09, revision D.01,⁴² for calculations using the B3LYP functional or Gaussian 16, revision A.03, 44 for calculations using the ω B97X-D functional.

X-ray Crystallographic Details. Diffraction-quality crystals of **Ag-1** were obtained by the slow vapor diffusion of hexane into a toluene solution of the compound to afford red needles. Diffraction-quality crystals of **Ag-2** and **6** were obtained from a toluene solution of the compound at -30 °C in a nitrogen atmosphere glovebox, affording crystals of **Ag-2** as red plates and crystals of **6** as violet plates. X-ray diffraction data for **Ag-2** were collected on a Bruker three-circle platform goniometer equipped with an Apex II CCD and an Oxford cryostream cooling device at 100 K. Radiation was generated from a graphite fine-focus sealed-tube Mo K α source (0.71073 Å). X-ray diffraction data for **Ag-1** and **6** were collected on a vertically mounted Bruker D8 three-circle platform goniometer equipped with an Apex II CCD and an Oxford Diffraction Helijet cooling device (15 K) with synchrotron radiation (0.41328 Å) supplied by ChemMatCARS, located at the Advanced Photon Source

(APS), Argonne National Laboratory (ANL). For all samples, crystals were mounted on a glass fiber using Paratone-N oil. Data were collected as a series of φ and ω scans, integrated using SAINT, ⁵⁸ and scaled with a multiscan absorption correction using SADABS. The structure was solved by intrinsic phasing methods using SHELXS-97 and refined against F^2 on all data by full-matrix least squares with SHELXL-97. All non-H atoms were refined anisotropically. H atoms were placed at idealized positions and refined using a riding model.

RESULTS

Synthesis and Characterization of Monomeric Silver **Corroles.** The silver complex Ag-1 and the 2,3,17,18tetrabromo derivative Ag-1-Br4 were prepared by treating the free-base corrole³³ with Ag(OAc) in pyridine, following literature procedures.²² The ¹H and ¹⁹F NMR spectra of both compounds exhibit sharp, well-resolved signals, which indicate that the compounds are diamagnetic. Interestingly, coupling of the β -pyrrole protons to the $^{107/109}$ Ag center is observed in the ¹H NMR spectrum (Figure S1). The ~0.7 Hz four-bond coupling constants are consistent with reported values (0.4-1.8~Hz). This coupling can be leveraged to determine 109Ag chemical shifts via two-dimensional heteronuclear NMR experiments. The inherent insensitivity of direct ¹⁰⁹Ag detection can be overcome by exciting a coupled proton and transferring the magnetization to the 109Ag nucleus, significantly enhancing the signal.⁶⁰ A ¹H/¹⁰⁹Ag HMQC NMR experiment was performed to determine the 109Ag chemical shifts of Ag-1 and Ag-1-Br₄: 2518.7 and 2607.3 ppm, respectively (Figure S2). Saturated AgNO₃ was utilized as an external standard ($\delta = -59.0$). Variable-temperature (VT) ¹H NMR spectra exhibit nominal shifts over the 25–100 °C range, indicating the absence of low-lying triplet states (Figure

The absorption spectra of Ag-1 and Ag-1-Br₄ exhibit a Soret band at ~427 nm and Q bands in the 500–600 nm range (Figure S4). A vibrational progression is observed for the Q bands, with Q(0,0) at ~575 nm, Q(1,0) at ~537 nm, and Q(2,0) at ~500 nm. These transitions are separated by 1305 \pm 71 cm⁻¹, which is comparable to the energetic spacing reported for free-base (1277 \pm 63 cm⁻¹)³³ and gold (1306 \pm 36 cm⁻¹)⁶¹ corroles. As observed for the gold analogues, bromination results in a nominal red shift of the absorption spectrum. Weak emission was observed for Ag-1 at room temperature, exhibiting a broad feature centered at 665 nm (Figure S5).

The CV of Ag-1 was recorded in MeCN; analogous data for Ag-1-Br₄ could not be obtained because the compound is insufficiently soluble in MeCN. An irreversible reduction is observed at −1.9 V versus ferrocenium/ferrocene (Fc⁺/Fc; Figure S6a) and attributed to demetalation of the compound, as evidenced by the sharp peak around 0 V on the return scan, which is consistent with Ag(0) oxidation. When a smaller potential window (Figure 2) is scanned to avoid this irreversible process, a reversible reduction is observed at -1.04 V, which is shifted to significantly more negative potentials relative to the Cu complex $(-0.23 \text{ V})^{30}$ A reversible oxidation is observed at +0.56 V, and a quasi-reversible oxidation occurs at +1.06 V (Figure S6b); similar phenomena are observed for the copper corrole at +0.55 and +1.27 V, respectively.³⁰ Additional waves are observed on the return scan due to the incomplete reversibility of the second oxidation. Given the similarity of Ag-1 to the copper analogue, both oxidation features are assigned as corrole-based processes,

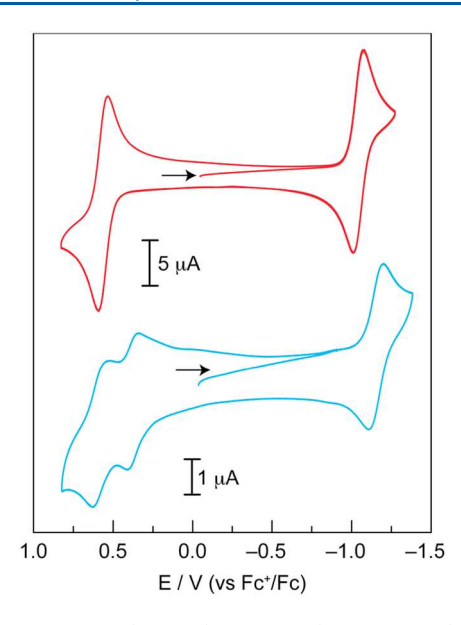


Figure 2. CVs of **Ag-1** (red line) and **Ag-2** (light-blue line) in MeCN with 0.1 M [TBA][PF₆] recorded at 100 mV s⁻¹ under a nitrogen atmosphere. Note that the current scales are different for the two CVs.

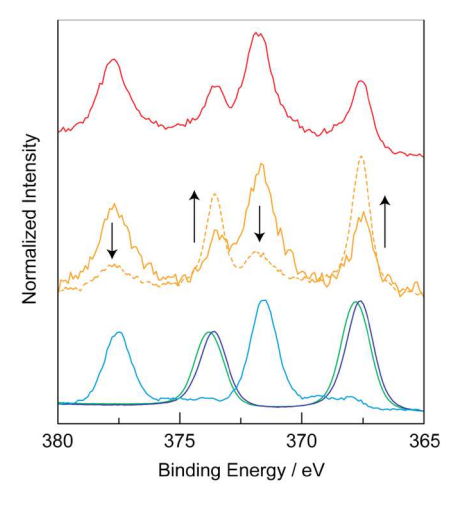


Figure 3. Ag 3d region of the XPS spectra of **Ag-1** (red line), **Ag-1-Br**₄ (yellow line), and reference compounds of varying oxidation state: AgF (green line), AgF₂ (dark-blue line), $[TBA][Ag(CF_3)_4]$ (light-blue line). Under prolonged X-ray exposure, **Ag-1-Br**₄ is readily reduced (dotted lines).

consistent with previous electrochemical studies. Because the reduction significantly differs from the copper analogue, this processes is assigned to be metal-centered [i.e., Ag(III)/Ag(II) couple].

XPS was utilized to determine the oxidation state of the Ag center in Ag-1 and Ag-1-Br₄ (Figure 3). First, a series of reference compounds of varying oxidation state were examined (Figure 3, lower traces): AgF, AgF₂, and [TBA][Ag(CF₃)₄]. Both Ag(I) and Ag(II) have similar binding energies, with Ag(II) having a slightly lower binding energy; the Ag $3d_{5/2}$ peaks are observed at 367.8 and 367.6 eV for AgF and AgF₂, respectively. As observed for [TBA][Cu(CF₃)₄], the peaks for the silver analogue are shifted to significantly higher binding energy, exhibiting a Ag $3d_{5/2}$ peak at 371.6 eV. Both corroles display two sets of peaks due to the presence of the photoreduced product. This is readily seen for Ag-1-Br₄, where

the initial spectrum with fewer scans (solid line) evolves to a new spectrum where the intensity of the lower-energy peaks for each transition increases (dashed line). Both corroles display nearly identical spectra, with the $3d_{5/2}$ and $3d_{3/2}$ peaks observed at 371.8 and 377.7 eV, respectively. These values are nearly identical with those reported for the silver complex of triphenylcorrole (371.70 and 377.66 eV)²² and have binding energies comparable to that of [TBA][Ag(CF₃)₄].

Diffraction-quality crystals of Ag-1 were grown from toluene to produce fine red needles. The solid-state structure is depicted in Figure 4, and the crystallographic data are

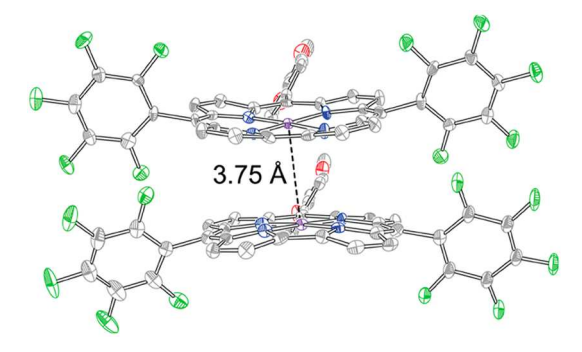


Figure 4. Solid-state structure of **Ag-1**. Thermal ellipsoids are drawn at the 50% probability level. H atoms and solvent molecules have been removed for clarity.

summarized in Table S1. Thermal ellipsoids are drawn at the 50% probability level; solvents of crystallization and H atoms have been removed for clarity. There are two silver corroles in the asymmetric unit, each with complementary conformations; the two macrocycles are domed such that the metal centers are proximal, giving a Ag···Ag distance of 3.75 Å. Additionally, π stacking interactions of the pentafluorophenyl substituents likely contribute to the dimeric structure. The Ag-N bond distances range from 1.940 to 1.959 Å with an average distance of 1.949 Å. The N-Ag-N bond angles range from 79.94° to 95.71°. The five atoms of each AgN₄ unit are nearly coplanar, with a maximum displacement of 0.025 Å from the mean N₄ plane, and the two N₄ planes exhibit an 11.98° interplanar angle. The bowl shape of the macrocycle gives rise to average displacements of 0.115 \pm 0.074 and 0.099 \pm 0.068 Å from the mean 23-atom plane of the corrole. The domed conformation of the macrocycle is rare for metallocorroles that lack an axial ligand and/or exhibit square-planar geometry, with the metal residing largely in the corrole plane. 62,63 Table S2 provides a comparison of the structural metrics for previously reported silver corrole complexes. The corrole conformation in Ag-1 is unique among structurally characterized silver corrole complexes, which all exhibit a saddled conformation.

Synthesis and Characterization of Pacman Corroles. To determine if this dimeric structure is a consequence of an authentic metal···metal interaction or simply a crystal packing effect, the analogous cofacial corrole dyad or "pacman" derivative was prepared. While cofacial porphyrin–corrole and corrole–corrole dyads have been previously reported, the corrole in the majority of these constructs has four β-phenyl substituents. Consequently, these very electron-rich macrocycles are not particularly stable in solution. The few examples of *meso*-substituted corrole–porphyrin 67,68 and corrole–corrole 69,70 dyads bear electron-donating mesityl substituents. It has been shown that corroles with penta-

Scheme 1. Synthetic Routes to the Monomeric Corrole 5 and Pacman Corrole 2

fluorophenyl substituents are extremely stable⁷¹ because these electron-withdrawing groups offset the inherent electron-richness of the corrole core.⁷² In an attempt to furnish a more stable pacman corrole, the synthesis of 2 (Scheme 1) was targeted.

The diformylxanthene backbone 4 was prepared from the commercially available dibromide. The HCl-catalyzed condensation of compound 4 and 5-pentafluorophenyldipyrromethane was performed following the procedure of Koszarna and Gryko.⁷³ In this case, only the monomeric corrole derivative 5 was isolated, preserving one of the formyl groups of the xanthene backbone. The target pacman 2 was obtained through a TFA-catalyzed condensation, following a modified literature procedure.⁷⁰ In this case, both the monomer 5 and the target pacman 2 were isolated. Metalation was accomplished using Ag(OAc) in pyridine to furnish the silver complex Ag-2 in high yield. The ¹⁰⁹Ag chemical shift for Ag-2 is 2514.7 ppm, as determined using a ¹H/¹⁰⁹Ag HMQC NMR experiment (Figure S7).

The solid-state structure of Ag-2 (Figure 5 and Table S1) is similar to that of Ag-1. The Ag-N bond distances range from 1.909 to 1.970 Å with an average distance of 1.942 Å. The N-Ag-N bond angles range from 80.96° to 95.80°. Other structural metrics are compiled in Table S2, drawing comparisons to Ag-1 and other previously reported silver corrole complexes. The two corrole units are complementarily bowled to yield a short 3.670 Å distance between the two Ag centers; this is nearly identical with the 3.659 Å distance observed for the $[SbF_6]^-$ salt of Ag-3. To achieve this configuration, the xanthene backbone significantly compresses to give a 146° angle between the 4-C, O, and 5-C of the xanthene spacer, which is significantly contracted from the expected linear arrangement (~180°) of these atoms. 74 Indeed, the backbone of Ag-2 is more compressed than xanthene-bridged cofacial metalloporphyrins, 75 which exhibit a 163-175° angle for the nickel(II), copper(II), and zinc(II) complexes. This demonstrates the flexibility of the xanthene backbone in cofacial corrole dyads and suggests that there is a significant driving force for the Ag···Ag interaction.

The CV of Ag-2 (Figure 2) exhibits a reversible reduction and two reversible oxidations. The reduction event for the pacman derivative is similar to Ag-1 but is shifted by ~ 100 mV

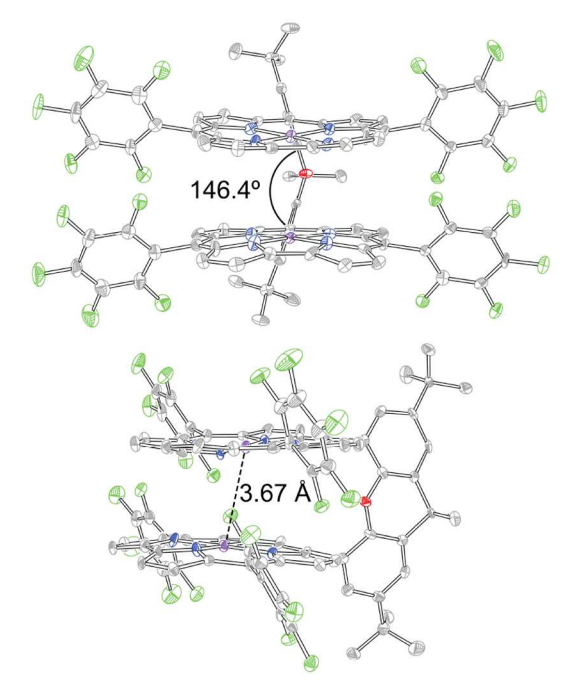


Figure 5. Solid-state structure of **Ag-2**. Thermal ellipsoids are drawn at the 50% probability level. H atoms and solvent molecules have been removed for clarity.

to more negative potentials (-1.15 V vs Fc⁺/Fc). Ag-2 exhibits two oxidation waves that are separated by \sim 200 mV; the first oxidation event occurs at +0.38 V and is 180 mV more negative than Ag-1. This splitting of the oxidation wave is indicative of a strong interaction between the corrole subunits, which has been observed for pacman porphyrins with a xanthene spacer, ^{76,77} as well as a cofacial antimony(V) bis(μ -oxo)corrole dimer. While the oxidation of Ag-2 occurs in one-electron steps, the reduction is a two-electron process. The height of the reduction wave is \sim 2.3 μ A (Figure 2), which is nearly twice that of the oxidation waves (1.2 μ A), corroborating this assignment. When a larger potential window is scanned (Figure S8), stepwise reduction of the corroles is not observed. This result is consistent with previous observations of cofacial porphyrins, where ring oxidation

Figure 6. Solid-state structure of **6.** Thermal ellipsoids are drawn at the 50% probability level. H atoms and solvent molecules have been removed for clarity. Additionally, pentafluorophenyl substituents have been removed from the *meso-C* atoms highlighted in magenta.

occurs in two one-electron steps and ring reduction occurs in a single two-electron process when the macrocycles are sufficiently proximate. On the basis of the spectroscopic and electrochemical analyses of various cofacial porphyrin architectures, Collman proposed that the dyad acts as a single redox-active entity with mixed-valence behavior. The first oxidation yields a π -based radical cation delocalized over both macrocycles. Upon the second oxidation, the two delocalized electrons become paired, giving rise to a nonclassical π -bonding interaction. Collman also concluded that successive reductions increase π -ring repulsion in the dimers, which is significant enough to minimize the interaction between the porphyrin rings, thus resulting in a single two-electron wave.

Next, Au-2 was prepared to determine if these structural phenomena were also observed for the gold complex and to compare the Au...Au distance to known examples of Au(III)... Au(III) aurophilic interactions. Typical gold metalation procedures 61,80 yielded the target complex, as well as the monometalated derivative, which coelutes with Au-2. Crystals suitable for X-ray diffraction were grown, but, surprisingly, the structure of octaphyrin 6 was obtained (Figure 6 and Table S1) rather than Au-2. The mother liquor from the crystallization was analyzed by thin-layer chromatography and revealed the presence of two compounds. The first, red fraction was identified as Au-2, while the second, green-brown fraction was identified as octaphyrin 6. The ¹H NMR spectrum exhibits a broad singlet at $\delta = 12.98$ for the *N*-pyrrole protons, demonstrating that the compound is not aromatic. This is corroborated by the β -pyrrole protons, which appear in the δ = 6-8 region, shifted upfield relative to those of the aromatic corrole (δ = 8.5–9.5). The solid-state structure of **6** exhibits a figure-eight motif, giving a twisted Hückel configuration rather

Chart 2. Isomers of [34]Octaphyrin(1.1.1.0.1.1.1.0)

than Möbius topology. 81–83 Given these data, as well as the similarity to the literature reports, 84,85 6 is assigned as [34] octaphyrin (1.1.1.0.1.1.1.0). Compound 6 is a novel isomer of this octaphyrin (Chart 2); derivatives reported by Vogel et al. 84 and Geier and Grindrod 85 cross over the bipyrrole linkage (7) rather than at the *meso* positions, as in 6. While the origin of this molecule is unclear, it is likely that the xanthene backbone templates the synthesis, enabling 6 to adopt this unique geometry. The absorption spectrum of 6 (Figure S9) exhibits a sharp feature at 715 nm and weaker transitions in the near-IR (900–1200 nm), similar to other derivatives of [34] octaphyrin (1.1.1.0.1.1.1.0).

DFT Calculations. Ghosh and co-workers have posited that the corrole ligand is on the edge of being noninnocent for silver complexes, depending on the peripheral substitution of the ligand.²³ They found that the corrole ligand was noninnocent in the case of β -octabromosilver corroles [i.e., a silver(II) corrole radical cation, analogous to copper corroles], while it was innocent in the case of β -unsubstituted corroles [i.e., an authentic Ag(III) complex]. These conclusions were supported by absorption spectroscopy and DFT calculations.⁸⁷ For the noninnocent complexes, calculations showed that the

Ag $d_{x^2-y^2}$ orbital is highly mixed with the corrole highest occupied molecular orbital (HOMO), as observed for copper corroles.²³ Subsequent Ag L-edge XANES experiments confirmed these assignments.²⁴

Ghosh's computational results suggest that the electronic structure of silver corroles may be tuned by modulating the energy of the corrole orbitals. Computationally, we surveyed other substitution patterns that could potentially exhibit noninnocence: Ag-1-Br₄, Ag-1-Br₈, and Ag-1-F₈. For each compound, three spin scenarios were calculated: a spinrestricted singlet [i.e., authentic Ag(III) complex], a spinunrestricted, broken-symmetry singlet [i.e., antiferromagnetically coupled silver(II) corrole radical cation, and a spinunrestricted triplet [i.e., ferromagnetically coupled silver(II) corrole radical cation]. These calculations were performed using the B3LYP functional with the 6-311G(d,p) basis set for all light atoms, a Wood-Boring quasi-relativistic effective core potential (i.e., MWB28) for Ag and Br, and a toluene CPCM solvation model. Cartesian coordinates for the optimized geometries are presented in Tables S3-S10. The results of these calculations are summarized in Figure 7, which depicts

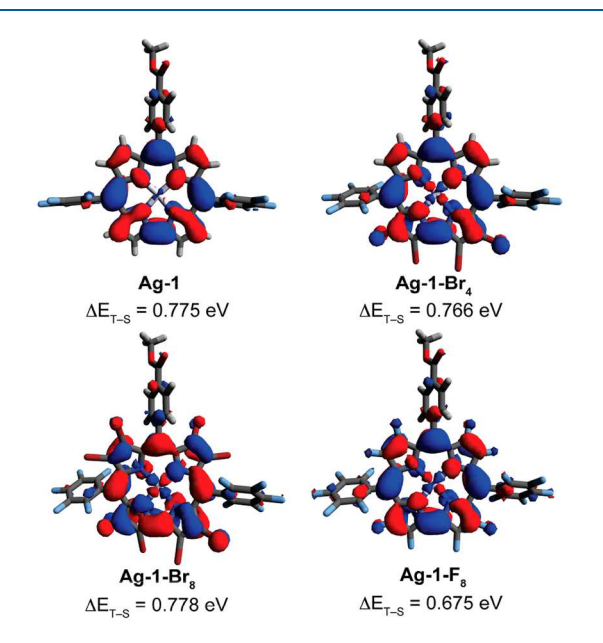


Figure 7. Summary of DFT calculations for derivatives of **Ag-1**, showing the HOMO for the spin-restricted calculations and ΔE_{T-S} . For β -substituted corroles, the Ag $\mathrm{d}_{x^2-y^2}$ orbital is highly mixed with the corrole HOMO.

the HOMO for each derivative and reports the triplet—singlet energy gap (ΔE_{T-S}). In all cases, the spin-unrestricted singlet calculation converges to the spin-restricted case, leaving no residual spin density. The parent silver corrole **Ag-1** does not display mixing of the Ag $d_{x^2-y^2}$ orbital and corrole HOMO, while the β -substituted derivatives (**Ag-1-Br**₄, **Ag-1-Br**₈, and **Ag-1-F**₈) do, consistent with Ghosh's results. ²³ In all cases, the triplet state is calculated to be significantly higher in energy for the silver complexes (0.68–0.78 eV) relative to the copper complex (0.017 eV) using the same computational methods. ³⁰ These results suggest that the triplet states are prohibitively high in energy to induce any meaningful shifts by VT NMR, consistent with experimental observations.

DFT calculations were used to corroborate the electrochemistry of Ag-1 and assign the electronic structure of these derivatives (Figure 8). Cartesian coordinates for the optimized geometries are presented in Tables S11-S14. The ground state of Ag-1 is best described as a Ag(III) complex with an innocent corrole ligand. The one-electron reduction and oxidation events were calculated as open-shell doublets, and the spin-density plots for these derivatives are shown in Figure 8. The reduction is metal-based, yielding a spin-density plot with one electron in the $d_{x^2-y^2}$ orbital. Conversely, the oxidation is corrole-based, with one electron in the corrole b₁ HOMO. For the doubly oxidized corrole, three spin scenarios were considered: a spin-restricted singlet, a spinunrestricted (i.e., broken-symmetry) singlet, and a spinunrestricted triplet. It was found that the two singlet calculations produced the same result and were 0.140 eV lower in energy than the triplet state. The HOMO for $[Ag-1]^{2+}$ corresponds to the canonical corrole HOMO-1 orbital of a2 symmetry, confirming that this redox event is ligand-based, precluding the formation of a Ag(IV) species.

To examine the interaction between Ag centers, DFT calculations were performed using both the B3LYP and ω B97X-D functionals; the latter includes dispersion corrections and accounts for long-range interactions. The structural metrics for the computed and experimental structures are summarized in Table 1. The dimeric nature of **Ag-1** was investigated by performing a geometry optimization with two molecules stacked in a cofacial arrangement (Tables S15 and S16). It was found that the ω B97X-D functional best recapitulates the experimental structure of **Ag-1** (Table S17) with an optimized Ag···Ag distance of 3.63 Å, whereas the B3LYP functional optimizes the dimer configuration with a significantly longer 5.84 Å Ag···Ag distance. Nevertheless, the dimeric structure is lower in energy than two independent molecules of **Ag-1**: 0.265 eV (6.11 kcal mol⁻¹) with B3LYP

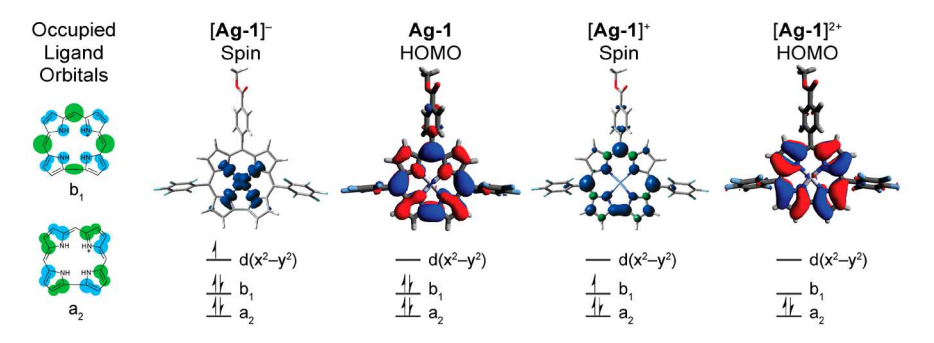


Figure 8. Summary of the results of DFT calculations for the oxidized and reduced derivatives of Ag-1. A qualitative molecular orbital diagram is provided to illustrate orbital occupancy. For reference, the canonical occupied corrole orbitals are included.

Table 1. Summary of the Structural and Computational Parameters Analyzing the Ag···Ag Interaction

		functional	Ag···Ag (Å)	Ct···Ct (Å) ^a	IA (deg) ^b	SA (deg) ^c	LS (Å) ^d	ВСР	$ \rho(r) $ (a.u.) ^e	$ abla^2[ho(r)] $ (a.u.)	DI ^g	WBI ^h
Ag-1	X-ray	B3LYP	3.75	3.78	7.24	23.8	1.52	no			0.0178	0.0242
Ag-1	X-ray	ω B97X-D	3.75	3.78	7.24	23.8	1.52	no			0.0171	0.0230
Ag-1	DFT	B3LYP	5.84	5.83	4.74	14.3	1.44	(3, -1)	0.0001	0.0003	0.0005	0.0014
Ag-1	DFT	ω B97X-D	3.63	3.67	3.77	24.3	1.51	no			0.0232	0.0178
Ag-2	X-ray	B3LYP	3.67	3.70	3.74	12.5	0.80	(3, -1)	0.0055	0.0170	0.0308	0.0317
Ag-2	X-ray	ω B97X-D	3.67	3.70	3.74	12.5	0.80	(3, -1)	0.0054	0.0168	0.0297	0.0301
Ag-2	DFT	B3LYP	5.07	5.11	9.61	12.8	1.13	(3, -1)	0.0005	0.0013	0.0022	0.0034
Ag-2	DFT	ω B97X-D	3.57	3.63	5.81	16.9	1.06	(3, -1)	0.0066	0.0212	0.0325	0.0342
Ag-3	X-ray ⁱ	B3LYP	3.66	3.71	2.94	24.4	1.53	(3, -1)	0.0058	0.0181	0.0241	0.0341
Ag-3	X-ray ⁱ	ω B97X-D	3.66	3.71	2.94	24.4	1.53	(3, -1)	0.0058	0.0180	0.0231	0.0324
Ag-3 ^j	X-ray ^k	B97D	3.46	3.33 ¹		16.2 ^m	0.96	yes	0.011^{n}			0.07^{n}
Ag-4°	X-ray ^p	M06	3.61	3.39 ¹		22.8 ^m	1.42	(3, -1)	0.0045	0.0174		
$[\mathbf{Ag-4}]^{+o}$	X-ray ^q	M06	3.53	3.31 ¹		23.2^{m}	1.41	(3, -1)	0.0051	0.0204		
$[Ag-4]^{2+o}$	X-ray ^r	M06	3.45	3.32 ¹		17.8 ^m	1.07	(3, -1)	0.0187	0.0351		

^aCenter-to-center distance between the centroids of the N_4 unit. ^bInterplanar angle, defined as the angle between the mean 23-atom plane (or 24-atom plane in the case of **Ag-3**) of the two macrocycles. ^cSlip angle (α), defined as the average angle between the vector normal to the N_4 plane and the Ag···Ag vector. ^dLateral shift between the two Ag centers, defined as $(\sin \alpha)(\text{Ct···Ct} \text{ distance})$. ^cElectronic density at the BCP in atomic units. ^fLaplacian of the electronic density in atomic units. ^gElectron delocalization index between Ag centers (i.e., average number of electrons shared between the two Ag ions) from Bader analysis. ^hWiberg bond index from NBO analysis. ⁱ[SbF₆] salt, CCDC 1536021. ^jData reproduced from ref 20. ^k[PF₆] salt, CCDC 1536020. ^lCenter-to-center distance between mean 24-atom planes. ^mAngle between the vector normal to the mean 24-atom plane and the Ct···Ct vector. ⁿCalculated for the DFT-optimized geometry. ^oData reproduced from ref 21. ^pCCDC 1907233. ^qCCDC 1907234. ^rCCDC 1907235.

and 2.045 eV (47.16 kcal mol⁻¹) with ω B97X-D. This result demonstrates that there is a significant driving force for dimerization, and the ω B97X-D functional best captures this dispersion interaction. Similarly, the geometry of **Ag-2** was optimized using both the B3LYP and ω B97X-D functionals (Tables S18 and S19). Again, the ω B97X-D functional best captures the solid-state geometry of **Ag-2** (Table S20), optimizing a Ag···Ag distance of 3.57 Å, whereas B3LYP predicts a relaxed, elongated structure (5.07 Å between metal centers).

A Bader analysis⁵¹ (i.e., atoms in molecules or AIM) was performed using the AIMAll program⁵³ to identify interactions between the Ag centers in Ag-1 and Ag-2. Complementary NBO analysis⁵⁵ was also performed, and the Wiberg bond index (WBI)⁵⁴ between the metal centers was determined. These calculations were performed for both DFT-optimized and experimental geometries using the B3LYP and ω B97X-D functionals; the results are summarized in Table 1. When the experimental solid-state structure is analyzed, the B3LYP and ωB97X-D functionals yield similar results. Analysis of the crystal structure of Ag-1 did not identify a bond critical point (BCP) between the Ag centers. A BCP of type (3, -1) was located between the two Ag atoms only for the B3LYPoptimized geometry, with the electronic density $\rho(r) = 1.22 \times$ 10^{-4} and Laplacian of electronic density $\nabla^2[\rho(r)] = 3.42 \times$ 10⁻⁴. The two Ag centers exhibit a delocalization index (DI) of 4.7×10^{-4} . The DI is identical to the bond order when two atoms are connected by a bond path, which is the atomic interaction line that joins two atoms, serving as a "bridge" of electron density. This quantifiable quantum-mechanical entity denotes a bonding interaction between atoms. The presence of both a bond path and a critical point is necessary and sufficient for two atoms to be bonded.8

Conversely, a Bader analysis identifies a (3, -1) type BCP between Ag centers in Ag-2 for all structures. For the experimental structure, the electronic density at the BCP is $\rho(r) = 0.0055$ and the Laplacian of the electronic density is

 $\nabla^2[\rho(r)] = 0.0170$. The positive value of the Laplacian indicates that this is a closed-shell interaction between the two atoms. 90 The values of these parameters are smaller than those reported for Ag(I)···Ag(I) argentophilic interactions (Table S21). However, this may be expected as a consequence of the longer Ag···Ag distance in Ag-2 relative to the Ag(I) examples, given that both $\rho(r)$ and $\nabla^2[\rho(r)]$ are inversely correlated with the Ag...Ag distance (Figure S10a). The Wiberg bond order derived from NBO analysis was determined to be 0.032 for Ag-2 and is nearly identical with the DI calculated from the Bader analysis. This value falls within the range reported for most Ag(I)···Ag(I) argentophilic interactions: 0.022-0.094 (Table S21). It should be noted that the Wiberg bond order does not correlate with the Ag...Ag distance (Figure S10b). Moreover, the metrics for the Ag···Ag interaction $[\rho(r), \nabla^2[\rho(r)],$ and WBI] in Ag-2 are similar to those for the $[SbF_6]^-$ salt of Ag-3 (Table S22), the first reported example of a Ag(III)...Ag(III) interaction, indicating that Ag-2 also exhibits this phenomenon. Table 1 also includes the structural metrics and computational analysis of the [PF₆] salt of Ag-3,²⁰ as well as Ag-4 in various oxidation states.²¹ Because different computational methods were used for these compounds, the metrics for the Bader and NBO analyses are not directly comparable. It should be noted that $\rho(r)$ and $\nabla^2[\rho(r)]$ increase with subsequent oxidations of Ag-4, reflecting stronger Ag...Ag interactions.

DISCUSSION

The electronic structure of silver corroles has been examined using a variety of complementary techniques including NMR, XPS, and electrochemistry in conjunction with DFT calculations. Our calculations are consistent with the results reported by Ghosh, ²³ demonstrating that β substitution induces mixing of the Ag $d_{x^2-y^2}$ orbital and corrole HOMO. The calculations also demonstrate that tetrabromination is sufficient to induce this mixing, suggesting that Ag-1 is an authentic Ag(III) complex, while Ag-1-Br₄ may be non-

innocent (i.e., silver(II) corrole radical cation). NMR studies of Ag-1 indicate that the ¹H NMR spectrum is similar to the Au complex, rather than the Cu derivative, further supporting the Ag(III) formulation. Because the room temperature ¹H NMR spectrum of Ag-1-Br₄ does not exhibit broadening or shifting of the signals relative to Ag-1 (as would be expected for a noninnocent complex), this compound is also likely a Ag(III) complex. VT NMR supports this assignment because neither Ag-1 nor Ag-1-Br₄ demonstrate significant temperature-dependent shifts. XPS analysis of the Ag 3d region for Ag-1 and Ag-1-Br₄ demonstrates that the spectra are nearly identical and have binding energies similar to those of [TBA][Ag(CF₃)₄], indicating that both corroles contain a Ag(III) center. To reconcile the experimentally observed Ag(III) and the calculated mixing of the Ag $d_{x^2-y^2}$ orbital and corrole HOMO in Ag-1-Br₄, we propose that peripheral substitution increases the covalency of the metal-ligand bond rather than modulating the electronic structure of the molecule.

For XPS studies, $[TBA][Ag(CF_3)_4]$ was utilized as a Ag(III)standard. The copper analogue has an inverted ligand field, giving rise to a Cu(I) complex rather than a Cu(III) species, as determined by X-ray spectroscopy. 91 Subsequent experimental studies confirm the presence of an inverted ligand field but suggest that a Cu(III) center is present in $[Cu(CF_3)_4]^{-.92}$ In the initial proposal of the inverted ligand field in trifluoromethyl complexes of coinage metals, 93 Snyder hypothesized that this same phenomenon would persist for the silver and gold derivatives.⁹⁴ Although this remains to be tested further experimentally, there is compelling evidence for the presence of a Ag(III) center in the [Ag(CF₃)₄]⁻ anion. In the initial report of this species, the complex was isolated as the silver(I) salt: Ag[Ag(CF₃)₄]. The ¹⁰⁹Ag NMR spectrum showed two resonances: a singlet at 368.2 ppm and a septet at 2232.6 ppm. The septet exhibits a coupling constant of 40.7 Hz, which is identical with that observed in the 19F NMR spectrum, indicating that this signal is due to the CF₃-bound Ag center. Because 109 Ag NMR is sensitive to the oxidation state, 60 these assignments are consistent with known chemical shifts of Ag(III) (δ > 2000). This chemical shift is likely not an artifact of the $-CF_3$ ligands because the $[Ag(CF_3)_2]^-$ anion exhibits a ¹⁰⁹Ag chemical shift of 565.5 ppm, ⁹⁶ falling in the range reported for Ag(I) complexes. ⁶⁰ The literature ¹⁰⁹Ag NMR data, in conjunction with the XPS data of Figure 3, suggest that [TBA][Ag(CF₃)₄] is an authentic Ag(III) complex. Recent computational and experimental studies support this formulation. 92,97 Although the complex does exhibit an inverted ligand field, the metal has a 3+ oxidation state.

The ¹⁰⁹Ag chemical shift further supports the Ag(III) assignment for the silver corrole complexes. By exploiting the coupling of the Ag center to the β-pyrrole protons (Figure S1), an HMQC NMR experiment was utilized for indirect ¹⁰⁹Ag detection. This overcomes the inherent difficulties of direct ¹⁰⁹Ag detection, which includes low sensitivity (10⁻⁴ relative to ¹H) and long relaxation times (minutes). ⁶⁰ The ¹⁰⁹Ag chemical shifts for Ag-1, Ag-1-Br₄, and Ag-2 are 2518.7, 2607.3, and 2514.7 ppm, respectively. The ~90 ppm downfield shift for Ag-1-Br₄ relative to Ag-1 likely reflects an inductive effect of the four bromo substituents. The similar chemical shifts for Ag-1 and Ag-2 indicate that the coordination environment of the Ag centers and the electronic structure of the complexes are nearly identical. To the best of our knowledge, this is the

first report of ¹⁰⁹Ag chemical shifts for silver porphyrinoids (i.e., tetrapyrrole and related macrocycles). It should be noted that ¹⁰⁹Ag NMR spectra have been previously reported for cryptands ⁹⁸ and other nonaromatic macrocyclic ligands. ⁹⁹

For canonical metallophilic interactions, the distance between metal centers is shorter than the sum of the van der Waals radii. However, the experimental Ag···Ag distances for Ag-1 (3.75 Å), Ag-2 (3.67 Å), and Ag-3 (3.66 Å) are longer than the radii of the two Ag centers: 3.44 Å. Similarly, the Au···Au distances observed for Au(III) aurophilic interactions in $[\mathrm{Me_4N}][\mathrm{Au}(\mathrm{N_3})_4]^{14}$ and $[\mathrm{Au}(\mathrm{bpy})\mathrm{Cl_2}][\mathrm{AuBr_4}],^{15}$ are 3.507 and 3.518 Å, respectively, which are both longer than the sum of the radii of two Au centers (3.32 Å). Indeed, the shortest examples of Au(III)···Au(III) aurophilic interactions (3.495 and 3.367 Å) 100,101 are still longer than the sum of the radii. It has been demonstrated computationally that the M···M distance increases with increasing oxidation state. Therefore, the Ag···Ag distance observed in Ag-2 is consistent with a Ag(III)···Ag(III) argentophilic interaction and is supported by theoretical calculations.

Complexes with metallophilic interactions often exhibit luminescence as a result of M···M interactions in the excited state. 102,103 This phenomenon has been observed for a variety of species with Ag(I)···Ag(I) argentophilic interactions, ¹⁷ and the emission features are typically quite broad (fwhm = 80-150 nm). 104,105 Although the luminescence is enhanced at low temperatures (<77 K), weak room-temperature emission has been observed. 105 In contrast to Ag(I)···Ag(I) argentophilic interactions, Ag-3 exhibits an unusually sharp emission feature (fwhm = 10 nm) centered at 546 nm at 77 K.²⁰ Analogous luminescence was not reported for Ag-4 derivatives.²¹ Weak emission was observed for Ag-1 at room temperature, exhibiting a broad (fwhm = 60 nm) feature centered at 665 nm. This broad emission is expected for M···M interactions and is consistent with photoluminescence from $Ag(I) \cdots Ag(I)$ argentophilic interactions, ^{17,104,105} unlike the unusually sharp emission feature reported for Ag-3.20 Emission from Ag-1 indicates that the Ag...Ag interaction persists in solution, making it the first example of an unsupported Ag(III)···Ag(III) argentophilic interaction.

The Ag···Ag interactions observed in the solid-state structures of **Ag-1** and **Ag-2** were examined computationally using Bader and NBO analyses. For both compounds, the DFT-optimized geometry using the ω B97X-D functional, which includes dispersion interactions, best represents the experimental geometry of the compounds. However, analysis of the experimental structures using the ω B97X-D and B3LYP functionals gives similar results (Table 1).

For Ag-1, the Bader analysis did not identify a BCP between the Ag centers for the experimental or ω B97X-D-optimized structures. This may be due to the large slip angle (~24°) between the two corrole units that diminishes the overlap between Ag centers. Interestingly, a BCP is identified for the B3LYP-optimized structure of Ag-1. Although the Ag···Ag distance is significantly extended (5.84 Å), the slip angle is smaller (~14°), resulting in a sufficient interaction to yield a BCP, albeit with very low electronic density. These results suggest that a combination of structural factors, not just the M···M distance, are determinant of metallophilic interactions. Even in the absence of a BCP, there is a nonzero interaction between the Ag centers, as evidenced by the DI and WBI.

Conversely, a BCP is identified between Ag centers for the calculated and experimental structures of Ag-2. This is due to

the decreased Ag···Ag distance and the reduced slip angle relative to Ag-1, resulting in increased orbital overlap of the Ag centers. The calculated electronic density $\rho(r)$ at the critical point is lower than that of previously reported Ag(I)···Ag(I) argentophilic interactions (Table S21). This is expected because $\rho(r)$ correlates with the Ag···Ag distance (Figure S10a), which is much shorter for Ag(I)···Ag(I) argentophilic interactions. The calculated WBI for the experimental structure of Ag-2 falls within the range reported for Ag(I)···Ag(I) argentophilic interactions (Table S21). Together, these computational results indicate that Ag-2 exhibits an authentic Ag(III)···Ag(III) argentophilic interaction.

In order to contextualize these computational results, comparisons may be drawn with the first reported example of a Ag(III)···Ag(III) argentophilic interaction: Ag-3.²⁰ The same computational methods as those used for Ag-1 and Ag-2 were used to analyze the solid-state structure of Ag-3 (as the [SbF₆] salt). Although the crystal structure exhibits a substantial ~24° slip angle between porphyrin units, the decreased Ag···Ag distance results in sufficient orbital overlap to yield a BCP between metal centers. The metrics for the Ag… Ag interaction $[\rho(r), \nabla^2[\rho(r)],$ and WBI] in Ag-3 are similar to those in Ag-2, further supporting the existence of an argentophilic interaction in the pacman corrole complex. A shorter Ag···Ag distance was observed for the [PF₆] salt of Ag-3. The 0.2 Å difference in the metal-metal distance with different counterions suggests that crystal packing effects may modulate the metallophilic interaction in Ag-3. Shorter Ag···Ag contacts are achieved with a more rigid ethene linker (Ag-4). The Ag...Ag distance decreases upon oxidation of the complex: 3.61 Å for Ag(II)/Ag(II), 3.53 Å for mixed-valent Ag(II)/ Ag(III), and 3.45 Å for Ag(III)/Ag(III). Consequently, the strength of the Ag...Ag interaction increases, as determined by a Bader analysis. It should be noted that only the doubly oxidized Ag(III)/Ag(III) derivative [Ag-4]²⁺ reflects a closedshell, metallophilic interaction. Other noncovalent, supramolecular interactions (e.g., π -stacking and hydrophobic interactions) likely contribute to the calculated Ag···Ag interaction in Ag-4 and [Ag-4]+.

The dimeric structures of Ag-1 and Ag-2 are enabled by various noncovalent, supramolecular interactions, including metallophilic and π -stacking interactions. Theoretical calculations confirm the presence of a closed-shell dispersion interaction between metal centers, reflective of a metallophilic interaction. While this does not necessarily reflect the dominant driving force for dimerization, it is certainly present. The argentophilic interaction is experimentally reflected by compression of the backbone in Ag-2. The 146° angle of the xanthene backbone is significantly smaller than the 163-175° angle previously observed for cofacial Ni(II), Cu(II), and Zn(II) porphyrins with a xanthene backbone. This suggests that there are additional stabilizing interactions in Ag-2 beyond π -stacking interactions between macrocycles that are absent in the porphyrin examples [i.e., the Ag(III)...Ag(III) argentophilic interaction]. Additionally, the semirigid xanthene backbone helps to minimize the slip angle and lateral shift between Ag centers. A comparison of the structural metrics of Table 1 reveals that the xanthene backbone affords greater overlap of the Ag centers relative to the flexible ethane or ethene linkers (Ag-3 and Ag-4).

While it is difficult to disentangle the energetic contribution of these noncovalent interactions, it may be inferred from the theoretical calculations. The energy stabilization of the dimeric structure of **Ag-1**, as calculated using the B3LYP functional, is 6.11 kcal mol⁻¹. This elongated structure with a 5.84 Å distance between Ag centers precludes the formation of significant π -stacking interactions. Despite the long Ag···Ag distance, the Bader analysis identifies a BCP between Ag centers, indicating that this structure captures the metallophilic interaction. In this limiting case, the stabilization energy of the **Ag-1** dimer is consistent with the 5–15 kcal mol⁻¹ range for argentophilic interactions. ¹⁷ Conversely, the energy stabilization of the dimeric structure calculated using the ω B97X-D functional is significantly larger: 47.16 kcal mol⁻¹. Because this method better accounts for intermolecular interactions, the stabilization energy reflects the sum of metallophilic, π -stacking, hydrophobic, and other noncovalent interactions.

CONCLUSION

Here, we have provided rare examples of Ag(III)···Ag(III) argentophilic interactions in silver corrole complexes. The monomeric complex Ag-1 exhibits a dimeric structure in the solid state. Although the Bader analysis does not identify a BCP between Ag atoms, there is a nonnegligible interaction between metal centers. Ag-1 exhibits weak emission, further supporting the presence of an argentophilic interaction in this complex. A pacman architecture (Ag-2) was then exploited to enforce a cofacial arrangement of two Ag(III) corroles. In the solid state, the Ag centers exhibit a close 3.67 Å contact. This metallophilic interaction results in significant compression of the xanthene backbone and an unusual domed conformation of the corrole. The Bader analysis identifies a BCP between the two metal centers in Ag-2, demonstrating that this is a closedshell dispersion interaction. The argentophilic interactions reported in this study form directly from Ag(III) complexes, as opposed to the oxidation of Ag(II) species to generate the Ag(III)···Ag(III) argentophilic interaction. ^{20,21} This study demonstrates that the xanthene backbone is sufficiently flexible to accommodate metallophilic interactions and may serve as a general platform to interrogate metal-metal interactions. This pacman corrole architecture can readily be extended to other, more flexible backbone spacers, such as diphenyl ether, ⁶⁸ to potentially enable closer M···M interactions. Similarly, a shorter rigid backbone, such as biphenylene, may help to maximize the overlap of the corrole macrocycles (i.e., minimize the slip angle and lateral shift), similar to xanthene, while decreasing the distance between metal centers.

The potential utility of Ag(III)...Ag(III) argentophilic interactions may be inferred from the reports of other metallophilic interactions, which can impart unique physical and optical properties. For example, $Ag_3[Co(CN)_6]$ exhibits "colossal" positive and negative thermal expansion that is an order of magnitude greater than typical crystalline materials. The Ag(I) ions are arranged in a hexagonal kagomé lattice with a \sim 3.5 Å distance between Ag centers. These argentophilic interactions impart flexibility in the lattice, which gives rise to this unique phenomenon. 107 Because many compounds with metallophilic interactions exhibit luminescence, perturbation of this emission could be leveraged for chemosensing applications. Pacman porphyrin architectures can bind guest molecules, such as 2-aminopyrimidine or the acridinium ion, 109 in the cleft between macrocycles. In both cases, guest binding modulates the photophysical properties of the pacman porphyrin. Cofacial corrole dyads analogous to Ag-2 could bind a guest molecule in the cleft to perturb the Ag(III)... Ag(III) interaction and quench any associated emission,

serving as a fluorescent turn-off sensor. The continued identification of novel platforms that support metallophilic interactions will allow molecules to be tailored for future applications.

ASSOCIATED CONTENT

Supporting Information

The Supporting Information is available free of charge at https://pubs.acs.org/doi/10.1021/acs.inorgchem.2c02285.

Summary of the crystallographic data, ¹H and ¹⁹F NMR spectra, other characterization data, and results of DFT calculations (PDF)

Accession Codes

CCDC 1046908, 1046909, and 2180997 contain the supplementary crystallographic data for this paper. These data can be obtained free of charge via www.ccdc.cam.ac.uk/data_request/cif, or by emailing data_request@ccdc.cam.ac.uk, or by contacting The Cambridge Crystallographic Data Centre, 12 Union Road, Cambridge CB2 1EZ, UK; fax: +44 1223 336033.

AUTHOR INFORMATION

Corresponding Authors

Daniel G. Nocera — Department of Chemistry and Chemical Biology, Harvard University, Cambridge, Massachusetts 02138, United States; ⊙ orcid.org/0000-0001-5055-320X; Email: dnocera@fas.harvard.edu

Christopher M. Lemon – Department of Chemistry and Chemical Biology, Harvard University, Cambridge, Massachusetts 02138, United States; Department of Chemistry and Biochemistry, Montana State University (MSU), Bozeman, Montana 59717, United States; orcid.org/0000-0001-9493-5488; Email: christopher.lemon1@montana.edu

Authors

David C. Powers — Department of Chemistry and Chemical Biology, Harvard University, Cambridge, Massachusetts 02138, United States; Present Address: Department of Chemistry, Texas A&M University, College Station, TX 77843; ⊚ orcid.org/0000-0003-3717-2001

Michael Huynh – Department of Chemistry and Chemical Biology, Harvard University, Cambridge, Massachusetts 02138, United States

Andrew G. Maher – Department of Chemistry and Chemical Biology, Harvard University, Cambridge, Massachusetts 02138, United States

Austin A. Phillips – Department of Chemistry and Biochemistry, Montana State University (MSU), Bozeman, Montana 59717, United States

Brian P. Tripet – Department of Chemistry and Biochemistry, Montana State University (MSU), Bozeman, Montana 59717, United States

Complete contact information is available at: https://pubs.acs.org/10.1021/acs.inorgchem.2c02285

Notes

The authors declare no competing financial interest.

ACKNOWLEDGMENTS

This material is based upon work supported by a grant from the National Science Foundation (Grant CHE-1855531). We are indebted to Dr. Dilek Dogutan for facilitating the completion of this study. C.M.L. acknowledges the National Science Foundation's Graduate Research Fellowship Program, the Miller Institute at University of California (UC) Berkeley for a Postdoctoral Fellowship, and The College of Letters & Science at MSU for startup funds. D.C.P. acknowledges a Ruth L. Kirschstein National Research Service award (F32GM103211). We thank Dr. Yu-Sheng Chen for assistance with X-ray crystallography at ChemMatCARS. ChemMat-CARS is principally supported by the Divisions of Chemistry (CHE) and Materials Research (DMR), National Science Foundation (NSF), under Grant NSF/CHE-1834750. Use of APS, an Office of Science User Facility operated for the U.S. Department of Energy (DOE), Office of Science by ANL, was supported by the U.S. DOE under Contract DE-AC02-06CH11357. Calculations run at Harvard (Gaussian 09) were performed using the Odyssey cluster supported by FAS Research Computing. Calculations run at UC Berkeley (Gaussian 16) were performed using the Molecular Graphics and Computation Facility, which is partially supported by National Institutes of Health (NIH) Grant S10OD023532. Computational time at UC Berkeley was funded by the Miller Institute. We thank Dr. Donald Smith for acquiring the mass spectrometry data. Funding for the Proteomics, Metabolomics, and Mass Spectrometry Facility at MSU was made possible in part by the MJ Murdock Charitable Trust, the NIH (under Awards P20GM103474 and S10OD028650), and the MSU Office of Research, Economic Development, and Graduate Education. The authors thank Prof. Erik Grumstrup for helpful discussions and for allowing them to utilize the Shimadzu spectrometer. Funding for the MSU Chemistry and Biochemistry NMR Center was made possible in part by the MJ Murdock Charitable Trust (under Award 2015066:MNL), the NSF (under Awards NSF-MRI:DBI-1532078 and NSF-MRI:CHE-2018388), and the Office of the Vice President for Research and Economic Development at MSU.

REFERENCES

- (1) Doerrer, L. H. Metallophilic Interactions in Double Salts: Toward 1D Metal Atom Chains. *Comments Inorg. Chem.* **2008**, 29, 93–127
- (2) Doerrer, L. H. Steric and Electronic Effects in Metallophilic Double Salts. *Dalton Trans.* **2010**, *39*, 3543–3553.
- (3) Pyykkö, P. Strong Closed-Shell Interactions in Inorganic Chemistry. *Chem. Rev.* **1997**, *97*, 597–636.
- (4) Schmidbaur, H.; Schier, A. A Briefing on Aurophilicity. Chem. Soc. Rev. 2008, 37, 1931–1951.
- (5) Schmidbaur, H.; Schier, A. Aurophilic Interactions as a Subject of Current Research: An Update. *Chem. Soc. Rev.* **2012**, *41*, 370–412.
- (6) Bondi, A. van der Waals Volumes and Radii. J. Phys. Chem. 1964, 68, 441–451.
- (7) Dahlen, M.; Seifert, T. P.; Lebedkin, S.; Gamer, M. T.; Kappes, M. M.; Roesky, P. W. Tetra- and Hexanuclear String Complexes of the Coinage Metals. *Chem. Commun.* **2021**, *57*, 13146–13149.
- (8) Kim, M.; Taylor, T. J.; Gabbaï, F. P. Hg(II)···Pd(II) Metallophilic Interactions. J. Am. Chem. Soc. 2008, 130, 6332–6333.
- (9) Campbell, M. G.; Powers, D. C.; Raynaud, J.; Graham, M. J.; Xie, P.; Lee, E.; Ritter, T. Synthesis and Structure of Solution-Stable One-Dimensional Palladium Wires. *Nat. Chem.* **2011**, *3*, 949–953.
- (10) Roundhill, D. M.; Gray, H. B.; Che, C.-M. Pyrophosphito-Bridged Diplatinum Chemistry. Acc. Chem. Res. 1989, 22, 55–61.
- (11) Gray, H. B.; Záliš, S.; Vlček, A. Electronic Structures and Photophysics of d⁸-d⁸ Complexes. *Coord. Chem. Rev.* **2017**, 345, 297–317.

- (12) Dos Remedios Pinto, M. A. F.; Sadler, P. J.; Neidle, S.; Sanderson, M. R.; Subbiah, A.; Kuroda, R. A Novel Di-Platinum(II) Octaphosphite Complex Showing Metal—Metal Bonding and Intense Luminescence; A Potential Probe for Basic Proteins. X-Ray Crystal and Molecular Structure. J. Chem. Soc., Chem. Commun. 1980, 0, 13—15.
- (13) Che, C.-M.; Butler, L. G.; Gray, H. B.; Crooks, R. M.; Woodruff, W. H. Metal—Metal Interactions in Binuclear Platinum(II) Diphosphite Complexes. Resonance Raman Spectra of the ${}^{1}A_{1g}(d\sigma^{*})^{2}$ and ${}^{3}A_{2u}(d\sigma^{*}p\sigma)$ Electronic State of $Pt_{2}(P_{2}O_{5}H_{2})_{4}^{4}$. *J. Am. Chem. Soc.* **1983**, *105*, 5492–5494.
- (14) Klapötke, T. M.; Krumm, B.; Galvez-Ruiz, J. C.; Nöth, H. Highly Sensitive Ammonium Tetraazidoaurates(III). *Inorg. Chem.* **2005**, *44*, 9625–9627.
- (15) Hayoun, R.; Zhong, D. K.; Rheingold, A. L.; Doerrer, L. H. Gold(III) and Platinum(II) Polypyridyl Double Salts and General Metathesis Route to Metallophilic Interactions. *Inorg. Chem.* **2006**, *45*, 6120–6122.
- (16) Mendizabal, F.; Pyykkö, P. Aurophilic Attraction in Binuclear Complexes with Au(I) and Au(III). A Theoretical Study. *Phys. Chem. Chem. Phys.* **2004**, *6*, 900–905.
- (17) Schmidbaur, H.; Schier, A. Argentophilic Interactions. *Angew. Chem., Int. Ed.* **2015**, *54*, 746–784.
- (18) Levason, W.; Spicer, M. D. The Chemistry of Copper and Silver in their Higher Oxidation States. *Coord. Chem. Rev.* **1987**, *76*, 45–120.
- (19) Ghosh, R. Chemistry of Silver(III) and Some of Its Compounds: A Review. J. Indian Chem. Soc. 2021, 98, 100238-5.
- (20) Singh, A. K.; Khan, F. S. T.; Rath, S. P. Silver(III)...Silver(III) Interactions that Stabilize the *syn* Form in a Porphyrin Dimer Upon Oxidation. *Angew. Chem., Int. Ed.* **2017**, *56*, 8849–8854.
- (21) Singh, A. K.; Usman, M.; Sciortino, G.; Garribba, E.; Rath, S. P. Through-Space Spin Coupling in a Silver(II) Porphyrin Dimer upon Stepwise Oxidations: Ag^{II}···Ag^{II}, Ag^{II}···Ag^{III}, and Ag^{III}···Ag^{III} Metallophilic Interactions. *Chem. Eur. J.* **2019**, *25*, 10098–10110.
- (22) Brückner, C.; Barta, C. A.; Briñas, R. P.; Krause Bauer, J. A. Synthesis and Structure of [meso-Triarylcorrolato]silver(III). Inorg. Chem. 2003, 42, 1673–1680.
- (23) Thomas, K. E.; Vazquez-Lima, H.; Fang, Y.; Song, Y.; Gagnon, K. J.; Beavers, C. M.; Kadish, K. M.; Ghosh, A. Ligand Noninnocence in Coinage Metal Corroles: A Silver Knife-Edge. *Chem. Eur. J.* **2015**, 21, 16839–16847.
- (24) Sarangi, R.; Giles, L. J.; Thomas, K. E.; Ghosh, A. Ligand Noninnocence in Silver Corroles: A XANES Investigation. *Eur. J. Inorg. Chem.* **2016**, 2016, 3225–3227.
- (25) Sinha, W.; Sommer, M. G.; Deibel, N.; Ehret, F.; Sarkar, B.; Kar, S. Silver Corrole Complexes: Unusual Oxidation States and Near-IR-Absorbing Dyes. *Chem. Eur. J.* **2014**, 20, 15920–15932.
- (26) Patra, B.; Sobottka, S.; Sinha, W.; Sarkar, B.; Kar, S. Isovalent Ag^{III}/Ag^{III} , Ag^{II}/Ag^{II} , Mixed-Valent Ag^{II}/Ag^{III} , and Corrolato-Based Mixed-Valency in β , β '-Linked [Bis{corrolato-silver}]ⁿ Complexes. *Chem. Eur. J.* **2017**, 23, 13858–13863.
- (27) Sahu, K.; Dutta, J.; Nayak, S.; Nayak, P.; Biswal, H. S.; Kar, S. Investigation of the Nature of Intermolecular Interactions in Tetra(thiocyanato)corrolato-Ag(III) Complexes: Agostic or Hydrogen Bonded? *Inorg. Chem.* **2022**, *61*, 6539–6546.
- (28) Bröring, M.; Brégier, F.; Cónsul Tejero, E. C.; Hell, C.; Holthausen, M. C. Revisiting the Electronic Ground State of Copper Corroles. *Angew. Chem., Int. Ed.* **2007**, *46*, 445–448.
- (29) Alemayehu, A. B.; Gonzalez, E.; Hansen, L. K.; Ghosh, A. Copper Corroles are Inherently Saddled. *Inorg. Chem.* **2009**, *48*, 7794–7799.
- (30) Lemon, C. M.; Huynh, M.; Maher, A. G.; Anderson, B. L.; Bloch, E. D.; Powers, D. C.; Nocera, D. G. Electronic Structure of Copper Corroles. *Angew. Chem., Int. Ed.* **2016**, *55*, 2176–2180.
- (31) Lim, H.; Thomas, K. E.; Hedman, B.; Hodgson, K. O.; Ghosh, A.; Solomon, E. I. X-ray Absorption Spectroscopy as a Probe of Ligand Noninnocence in Metallocorroles: The Case of Copper Corroles. *Inorg. Chem.* **2019**, *58*, 6722–6730.

- (32) Lemon, C. M.; Dogutan, D. K.; Nocera, D. G. Porphyrin and Corrole Platforms for Water Oxidation, Oxygen Reduction, and Peroxide Dismutation. In *Handbook of Porphyrin Science*; Kadish, K. M., Smith, K. M., Guilard, R.,, Eds.; World Scientific Publishing: Singapore, 2012; Vol. 21; pp 1–143.
- (33) Lemon, C. M.; Halbach, R. L.; Huynh, M.; Nocera, D. G. Photophysical Properties of β -Substituted Free-Base Corroles. *Inorg. Chem.* **2015**, *54*, 2713–2725.
- (34) Fulmer, G. R.; Miller, A. J. M.; Sherden, N. H.; Gottlieb, H. E.; Nudelman, A.; Stoltz, B. M.; Bercaw, J. E.; Goldberg, K. I. NMR Chemical Shifts of Trace Impurities: Common Laboratory Solvents, Organics, and Gases in Deuterated Solvents Relevant to the Organometallic Chemist. *Organometallics* **2010**, *29*, 2176–2179.
- (35) Penner, G. H.; Liu, X. Silver NMR Spectroscopy. Prog. Nucl. Magn. Reson. Spectrosc. 2006, 49, 151–167.
- (36) Watts, J. F.; Wolstenholme, J. An Introduction to Surface Analysis by XPS and AES; John Wiley and Sons: Chichester, U.K., 2003.
- (37) Barr, T. L.; Seal, S. J. Nature of the Use of Adventitious Carbon as a Binding Energy Standard. *J. Vac. Sci. Technol. A* **1995**, *13*, 1239–1246
- (38) Becke, A. D. Density-Functional Exchange-Energy Approximation with Correct Asymptotic Behavior. *Phys. Rev. A* **1988**, *38*, 3098–3100.
- (39) Becke, A. D. A New Mixing of Hartree–Fock and Local Density-Functional Theories. *J. Chem. Phys.* **1993**, 98, 1372–1377.
- (40) Becke, A. D. Density-Functional Thermochemistry. III. The Role of Exact Exchange. *J. Chem. Phys.* **1993**, *98*, 5648–5652.
- (41) Lee, C.; Yang, W.; Parr, R. G. Development of the Colle-Salvetti Correlation-Energy Formula into a Functional of the Electron Density. *Phys. Rev. B* **1988**, *37*, 785–789.
- (42) Frisch, M. J.; Trucks, G. W.; Schlegel, H. B.; Scuseria, G. E.; Robb, M. A.; Cheeseman, J. R.; Scalmani, G.; Barone, V.; Mennucci, B.; Petersson, G. A.; Nakatsuji, H.; Caricato, M.; Li, X.; Hratchian, H. P.; Izmaylov, A. F.; Bloino, J.; Zheng, G.; Sonnenberg, J. L.; Hada, M.; Ehara, M.; Toyota, K.; Fukuda, R.; Hasegawa, J.; Ishida, M.; Nakajima, T.; Honda, Y.; Kitao, O.; Nakai, H.; Vreven, T.; Montgomery, J. A., Jr.; Peralta, J. E.; Ogliaro, F.; Bearpark, M.; Heyd, J. J.; Brothers, E.; Kudin, K. N.; Staroverov, V. N.; Kobayashi, R.; Normand, J.; Raghavachari, K.; Rendell, A.; Burant, J. C.; Iyengar, S. S.; Tomasi, J.; Cossi, M.; Rega, N.; Millam, J. M.; Klene, M.; Knox, J. E.; Cross, J. B.; Bakken, V.; Adamo, C.; Jaramillo, J.; Gomperts, R.; Stratmann, R. E.; Yazyev, O.; Austin, A. J.; Cammi, R.; Pomelli, C.; Ochterski, J. W.; Martin, R. L.; Morokuma, K.; Zakrzewski, V. G.; Voth, G. A.; Salvador, P.; Dannenberg, J. J.; Dapprich, S.; Daniels, A. D.; Farkas, Ö.; Foresman, J. B.; Ortiz, J. V.; Cioslowski, J.; Fox, D. J. Gaussian 09, revision D.01; Gaussian, Inc.: Wallingford, CT, 2009.
- (43) Chai, J. D.; Head-Gordon, M. Long-Range Corrected Hybrid Density Functionals with Damped Atom—Atom Dispersion Corrections. *Phys. Chem. Chem. Phys.* **2008**, *10*, 6615–6620.
- (44) Frisch, M. J.; Trucks, G. W.; Schlegel, H. B.; Scuseria, G. E.; Robb, M. A.; Cheeseman, J. R.; Scalmani, G.; Barone, V.; Petersson, G. A.; Nakatsuji, H.; Li, X.; Caricato, M.; Marenich, A. V.; Bloino, J.; Janesko, B. G.; Gomperts, R.; Mennucci, B.; Hratchian, H. P.; Ortiz, J. V.; Izmaylov, A. F.; Sonnenberg, J. L.; Williams-Young, D.; Ding, F.; Lipparini, F.; Egidi, F.; Goings, J.; Peng, B.; Petrone, A.; Henderson, T.; Ranasinghe, D.; Zakrzewski, V. G.; Gao, J.; Rega, N.; Zheng, G.; Liang, W.; Hada, M.; Ehara, M.; Toyota, K.; Fukuda, R.; Hasegawa, J.; Ishida, M.; Nakajima, T.; Honda, Y.; Kitao, O.; Nakai, H.; Vreven, T.; Throssell, K.; Montgomery, J. A., Jr.; Peralta, J. E.; Ogliaro, F.; Bearpark, M. J.; Heyd, J. J.; Brothers, E. N.; Kudin, K. N.; Staroverov, V. N.; Keith, T. A.; Kobayashi, R.; Normand, J.; Raghavachari, K.; Rendell, A. P.; Burant, J. C.; Iyengar, S. S.; Tomasi, J.; Cossi, M.; Millam, J. M.; Klene, M.; Adamo, C.; Cammi, R.; Ochterski, J. W.; Martin, R. L.; Morokuma, K.; Farkas, Ö.; Foresman, J. B.; Fox, D. J. Gaussian 16, revision A.03; Gaussian, Inc.: Wallingford, CT, 2016.
- (45) Krishnan, R.; Binkley, J. S.; Seeger, R.; Pople, J. A. Self-Consistent Molecular Orbital Methods. XX. A Basis Set for Correlated Wave Functions. *J. Chem. Phys.* **1980**, 72, 650–654.

- (46) Frisch, M. J.; Pople, J. A.; Binkley, J. S. Self-Consistent Molecular Orbital Methods 25. Supplementary Functions for Gaussian Basis Sets. *J. Chem. Phys.* **1984**, *80*, 3265–3269.
- (47) Wood, J. H.; Boring, A. M. Improved Pauli Hamiltonian for Local-Potential Problems. *Phys. Rev. B* **1978**, *18*, 2701–2711.
- (48) Barone, V.; Cossi, M. Quantum Calculation of Molecular Energies and Energy Gradients in Solution by a Conductor Solvent Model. *J. Phys. Chem. A* **1998**, *102*, 1995–2001.
- (49) Cossi, M.; Rega, N.; Scalmani, G.; Barone, V. Energies, Structures, and Electronic Properties of Molecules in Solution with the C-PCM Solvation Model. *J. Comput. Chem.* **2003**, 24, 669–681.
- (50) Hanwell, M. D.; Curtis, D. E.; Lonie, D. C.; Vandermeersch, T.; Zurek, E.; Hutchison, G. R. Avogadro: An Advanced Semantic Chemical Editor, Visualization, and Analysis Platform. *J. Cheminform.* **2012**, *4*, 17.
- (51) Bader, R. F. W. Atoms in Molecules. Acc. Chem. Res. 1985, 18, 9–15.
- (52) Bader, R. F. W. Atoms in Molecules: A Quantum Theory; Oxford University Press: Oxford, U.K., 1990.
- (53) AİMAll, version 15.05.18; Todd, A., Keith, T. K., Eds.; Gristmill Software: Overland Park, KS, 2015; aim.tkgristmill.com.
- (54) Wiberg, K. B. Application of the Pople-Santry-Segal CNDO Method to the Cyclopropylcarbinyl and Cyclobutyl Cation and to Bicyclobutane. *Tetrahedron* **1968**, *24*, 1083–1096.
- (55) Foster, J. P.; Weinhold, F. Natural Hybrid Orbitals. J. Am. Chem. Soc. 1980, 102, 7211–7218.
- (56) Reed, A. E.; Curtiss, L. A.; Weinhold, F. Intermolecular Interactions from a Natural Bond Order, Donor-Acceptor Viewpoint. *Chem. Rev.* **1988**, *88*, 899–926.
- (57) Glendening, E. D; Reed, A. E.; Carpenter, J. E.; Weinhold, F. NBO 3.0 Program Manual; University of Wisconsin: Madison, WI, 1990; http://www.ccl.net/cca/software/NT/mopac6/nbo.htm.
- (58) Bruker, A. X. S. Apex II; Bruker AXS: Madison, WI, 2009.
- (59) Sheldrick, G. M. Experimental Phasing with SHELXC/D/E: Combining Chain Tracing with Density Modification. Acta Crystallogr., Sect. D: Biol. Crystallogr. 2010, D66, 479–485.
- (60) Zangger, K.; Armitage, I. M. Silver and Gold NMR. Met.-Based Drugs 1999, 6, 239-245.
- (61) Lemon, C. M.; Powers, D. C.; Brothers, P. J.; Nocera, D. G. Gold Corroles as Near-IR Phosphors for Oxygen Sensing. *Inorg. Chem.* **2017**, *56*, 10991–10997.
- (62) Thomas, K. E.; Alemayehu, A. B.; Conradie, J.; Beavers, C. M.; Ghosh, A. The Structural Chemistry of Metallocorroles: Combined X-ray Crystallography and Quantum Chemistry Studies Afford Unique Insights. *Acc. Chem. Res.* **2012**, *45*, 1203–1214.
- (63) Ghosh, A. Electronic Structure of Corrole Derivatives: Insights from Molecular Structures, Spectroscopy, Electrochemistry, and Quantum Chemical Calculations. *Chem. Rev.* **2017**, *117*, 3798–3881.
- (64) Jérôme, F.; Gros, C. P.; Tardieux, C.; Barbe, J. M.; Guilard, R. Synthesis of a 'Face-to-Face' Porphyrin-Corrole. A Potential Precursor of a Catalyst for the Four-Electron Reduction of Dioxygen. *New J. Chem.* 1998, 22, 1327–1329.
- (65) Kadish, K. M.; Frémond, L.; Ou, Z.; Shao, J.; Shi, C.; Anson, F. C.; Burdet, F.; Gros, C. P.; Barbe, J. M.; Guilard, R. Cobalt(III) Corroles as Electrocatalysts for the Reduction of Dioxygen: Reactivity of a Monocorrole, Biscorroles, and Porphyrin—Corrole Dyads. *J. Am. Chem. Soc.* 2005, 127, 5625—5631.
- (66) Kadish, K. M.; Ou, Z.; Shao, J.; Gros, C. P.; Barbe, J. M.; Jérôme, F.; Bolze, F.; Burdet, F.; Guilard, R. Alkyl and Aryl Substituted Corroles. 3. Reactions of Cofacial Cobalt Biscorroles and Porphyrin-Corroles with Pyridine and Carbon Monoxide. *Inorg. Chem.* 2002, 41, 3990–4005.
- (67) Barbe, J. M.; Burdet, F.; Espinosa, E.; Guilard, R. Synthesis and Physicochemical Characterization of Bis(macrocycles) Involving a Porphyrin and a *meso*-Substituted Corrole X-ray Crystal Structure of a [(Free-base porphyrin)—corrole]bis(pyridine)cobalt Complex. *Eur. J. Inorg. Chem.* **2005**, 2005, 1032—1041.
- (68) Gros, C. P.; Brisach, F.; Meristoudi, A.; Espinosa, E.; Guilard, R.; Harvey, P. D. Modulation of the Singlet-Singlet Through-Space

- Energy Transfer Rates in Cofacial Bisporphyrin and Porphyrin-Corrole Dyads. *Inorg. Chem.* **2007**, *46*, 125–135.
- (69) Pacholska, E.; Espinosa, E.; Guilard, R. New Route to a Faceto-Face Biscorrole Free-Base and the Corresponding Heterobimetallic Copper(III)—Silver(III) Complex. *Dalton Trans.* **2004**, 3181—3183.
- (70) El Ojaimi, M.; Gros, C. P.; Barbe, J. M. Efficient Two-Step Synthesis of Face-to-Face *meso*-Substituted Bis(corrole) Dyads. *Eur. J. Org. Chem.* **2008**, 2008, 1181–1186.
- (71) Geier, G. R.; Chick, J. F. B.; Callinan, J. B.; Reid, C. G.; Auguscinski, W. P A Survey of Acid Catalysis and Oxidation Conditions in the Two-Step, One-Flask Synthesis of Meso-Substituted Corroles via Dipyrromethanedicarbinols and Pyrrole. *J. Org. Chem.* **2004**, *69*, 4159–4169.
- (72) Gross, Z.; Gray, H. B. How Do Corroles Stabilize High Valent Metals? *Comments Inorg. Chem.* **2006**, *27*, 61–72.
- (73) Koszarna, B.; Gryko, D. T. Efficient Synthesis of meso-Substituted Corroles in a H₂O–MeOH Mixture. *J. Org. Chem.* **2006**, 71, 3707–3717.
- (74) Koo, B. J.; Huynh, M.; Halbach, R. L.; Stubbe, J.; Nocera, D. G. Modulation of Phenol Oxidation in Cofacial Dyads. *J. Am. Chem. Soc.* **2015**, *137*, 11860–11863.
- (75) Chang, C. J.; Deng, Y.; Heyduk, A. F.; Chang, C. K.; Nocera, D. G. Xanthene-Bridged Cofacial Bisporphyrins. *Inorg. Chem.* **2000**, *39*, 959–966.
- (76) Chang, C. J.; Deng, Y.; Shi, C.; Chang, C. K.; Anson, F. C.; Nocera, D. G. Electrocatalytic Four-Electron Reduction of Oxygen to Water by a Highly Flexible Cofacial Cobalt Bisporphyrin. *Chem. Commun.* **2000**, 1355–1356.
- (77) Loh, Z.-H.; Miller, S. E.; Chang, C. J.; Carpenter, S. D.; Nocera, D. G. Excited-State Dynamics of Cofacial Pacman Porphyrins. *J. Phys. Chem. A* **2002**, *106*, 11700–11708.
- (78) Lemon, C. M.; Maher, A. G.; Mazzotti, A. R.; Powers, D. C.; Nocera, D. G.; Gonzalez, M. I. Multielectron C–H Photoactivation with an Sb(V) Oxo Corrole. *Chem. Commun.* **2020**, *56*, 5247–5250.
- (79) Le Mest, Y.; L'Her, M.; Hendricks, N. H.; Kim, K.; Collman, J. P. Electrochemical and Spectroscopic Properties of Dimeric Cofacial Porphyrins with Nonelectroactive Metal Centers. Delocalization Processes in the Porphyrin π -Cation-Radical Systems. *Inorg. Chem.* **1992**, *31*, 835–847.
- (80) Thomas, K. E.; Alemayehu, A. B.; Conradie, J.; Beavers, C.; Ghosh, A. Synthesis and Molecular Structure of Gold Triarylcorroles. *Inorg. Chem.* **2011**, *50*, 12844–12851.
- (81) Jux, N. The Porphyrin Twist: Hückel and Möbius Aromaticity. *Angew. Chem., Int. Ed.* **2008**, 47, 2543–2546.
- (82) Yoon, Z. S.; Osuka, A.; Kim, D. Möbius Aromaticity and Antiaromaticity in Expanded Porphyrins. *Nat. Chem.* **2009**, *1*, 113–122
- (83) Osuka, A.; Saito, S. Expanded Porphyrins and Aromaticity. Chem. Commun. 2011, 47, 4330-4339.
- (84) Vogel, E.; Bröring, M.; Fink, J.; Rosen, D.; Schmickler, H.; Lex, J.; Chan, K. W. K.; Wu, Y. D.; Plattner, D. A.; Nendel, M.; Houk, K. N. From Porphyrin Isomers to Octapyrrolic "Figure Eight" Macrocycles. *Angew. Chem., Int. Ed. Engl.* 1995, 34, 2511–2514.
- (85) Geier, G. R.; Grindrod, S. C. Meso-Substituted [34]Octaphyrin (1.1.1.0.1.1.1.0) and Corrole Formation in Reactions of a Dipyrromethanedicarbinol with 2,2'-Bipyrrole. *J. Org. Chem.* **2004**, 69, 6404–6412.
- (86) Naoda, K.; Osuka, A. Structural and Aromaticity Control of [34]Octaphyrin(1.1.1.0.1.1.1.0) by Protonation and Deprotonation. *Asian J. Org. Chem.* **2017**, *6*, 1205–1208.
- (87) Ganguly, S.; Ghosh, A. Seven Clues to Ligand Noninnocence: The Metallocorrole Paradigm. Acc. Chem. Res. 2019, 52, 2003–2014.
- (88) Bader, R. F. W. A Bond Path: A Universal Indicator of Bonded Interactions. *J. Phys. Chem. A* **1998**, *102*, 7314–7323.
- (89) Bader, R. F. W. Bond Paths are Not Chemical Bonds. *J. Phys. Chem. A* **2009**, *113*, 10391–10396.
- (90) Munshi, P.; Guru Row, T. N. Evaluation of Weak Intermolecular Interactions in Molecular Crystals via Experimental

- and Theoretical Charge Densities. Crystallogr. Rev. 2005, 11, 199-241.
- (91) Walroth, R. C.; Lukens, J. T.; MacMillan, S. N.; Finkelstein, K. D.; Lancaster, K. M. Spectroscopic Evidence for a $3d^{10}$ Ground State Electronic Configuration and Ligand Field Inversion in $[Cu(CF_3)_4]^{1-}$. *J. Am. Chem. Soc.* **2016**, *138*, 1922–1931.
- (92) Baya, M.; Joven-Sancho, D.; Alonso, P. J.; Orduna, J.; Menjón, B. M—C Bond Homolysis in Coinage-Metal [M(CF₃)₄]⁻ Derivatives. *Angew. Chem., Int. Ed.* **2019**, *58*, 9954–9958.
- (93) Snyder, J. P. Elusiveness of Cu^{III} Complexation; Preference for Trifluoromethyl Oxidation in the Formation of [Cu^I(CF₃)₄]⁻ Salts. *Angew. Chem., Int. Ed. Engl.* **1995**, 34, 80–81.
- (94) Snyder, J. P. Distinguishing Copper d⁸ and d¹⁰ Configurations in a Highly Ionic Complex; A Nonformal Metal Oxidation State. *Angew. Chem., Int. Ed. Engl.* **1995**, 34, 986–987.
- (95) Dukat, W.; Naumann, D. Trifluormethyl-Silber-Verbindungen: Synthese und Struktur des Ag(III)-Komplexanions $[Ag(CF_3)_4]^-$. *Rev. Chim. Miner.* **1986**, 23, 589–603.
- (96) Eujen, R.; Hoge, B.; Brauer, D. J. Preparation and NMR Spectra of the (Trifluoromethyl)argentates(III) $[Ag(CF_3)_nX_{4-n}]^-$, with X = CN (n = 1-3), CH_3 , $C:CC_6H_{11}$, Cl, Br (n = 2, 3), and I (n = 3), and of Related Silver(III) Compounds. Structures of $[PPh_4][trans-Ag(CF_3)_2(CN)_2]$ and $[PPh_4][Ag(CF_3)_3(CH_3)]$. *Inorg. Chem.* **1997**, 36, 1464–1475.
- (97) Joven-Sancho, D.; Baya, M.; Martín, A.; Menjón, B. Homoleptic Trifluoromethyl Derivatives of Ag^{II} and Ag^{III}. *Chem. Eur. J.* **2018**, *24*, 13098–13101.
- (98) Drew, M. G. B.; Harding, C. J.; Howarth, O. W.; Lu, Q.; Marrs, D. J.; Morgan, G. G.; McKee, V.; Nelson, J. Thiophene-Linked Azacryptand Sites for Dicopper and Disilver; Thiophene Sulfur as an Inert Spacer? *J. Chem. Soc., Dalton Trans.* 1996, 3021–3030.
- (99) Font, M.; Acuña-Parés, F.; Parella, T.; Serra, J.; Luis, J. M.; Lloret-Fillol; Costas, M.; Ribas, X. Direct Observation of Two-Electron Ag(I)/Ag(III) Redox Cycles in Coupling Catalysis. *Nat. Commun.* **2014**, *5*, 4373.
- (100) Lu, W.; Chan, K. T.; Wu, S. X.; Chen, Y.; Che, C. M. Quest for an Intermolecular Au(III)····Au(III) Interaction Between Cyclometalated Gold(III) Cations. *Chem. Sci.* **2012**, *3*, 752–755.
- (101) Wan, Q.; Xia, J.; Lu, W.; Yang, J.; Che, C. M. Kinetically Controlled Self-Assembly of Phosphorescent Au^{III} Aggregates and Ligand-to-Metal—Metal Charge Transfer Excited State: A Combined Spectroscopic and DFT/TDDFT Study. *J. Am. Chem. Soc.* **2019**, *141*, 11572—11582.
- (102) Mauro, M.; Aliprandi, A.; Septiadi, D.; Kehr, N. S.; De Cola, L. When Self-Assembly Meets Biology: Luminescent Platinum Complexes for Imaging Applications. *Chem. Soc. Rev.* **2014**, *43*, 4144–4166.
- (103) Schmidbaur, H.; Raubenheimer, H. G. Excimer and Exciplex Formation in Gold(I) Complexes Preconditioned by Aurophilic Interactions. *Angew. Chem., Int. Ed.* **2020**, *59*, 14748–14771.
- (104) Yang, C.; Elbjeirami, O.; Gamage, C. S. P.; Dias, H. V. R.; Omary, M. A. Luminescence Enhancement and Tuning *via* Multiple Cooperative Supramolecular Interactions in an Ion-paired Multinuclear Complex. *Chem. Commun.* **2011**, *47*, 7434–7436.
- (105) Huang, R.-W.; Zhu, Y.; Zang, S.-Q.; Zhang, M.-L. Construction of Silver–Organic Framework with Silver Rods of Repeated Ag-Triangle Units: Synthesis, Structure, and Properties. *Inorg. Chem. Commun.* **2013**, 33, 38–42.
- (106) Goodwin, A. L.; Calleja, M.; Conterio, M. J.; Dove, M. T.; Evans, J. S. O.; Keen, D. A.; Peters, L.; Tucker, M. G. Colossal Positive and Negative Thermal Expansion in the Framework Material Ag₃[Co(CN)₆]. *Science* **2008**, *319*, 794–797.
- (107) Goodwin, A. L.; Keen, D. A.; Tucker, M. G.; Dove, M. T.; Peters, L.; Evans, J. S. O. Argentophilicity-Dependent Colossal Thermal Expansion in Extended Prussian Blue Analogues. *J. Am. Chem. Soc.* **2008**, *130*, 9660–9661.
- (108) Chang, C. J.; Loh, Z.-H.; Deng, Y.; Nocera, D. G. The Pacman Effect: A Supramolecular Strategy for Controlling the Excited-State

Dynamics of Pillared Cofacial Bisporphyrins. *Inorg. Chem.* **2003**, 42, 8262–8269.

(109) Tanaka, M.; Ohkubo, K.; Gros, C. P.; Guilard, R.; Fukuzumi, S. Persistent Electron-Transfer State of a π-Complex of Acridinium Ion Inserted between Porphyrin Rings of Cofacial Bisporphyrins. *J. Am. Chem. Soc.* **2006**, *128*, 14625–14633.

□ Recommended by ACS

Rh(I) and Organo-Rh(III) Complexes of *meso*-Triarylbiphenylcorrole

Sangya Chitranshi, A. Srinivasan, et al.

DECEMBER 19, 2022

INORGANIC CHEMISTRY

READ 🗹

Synthesis of Trimethyltriazacyclohexane (Me₃tach) Sandwich Complexes of Uranium, Neptunium, and Plutonium Triiodides: (Me₃tach)₂AnI₃

Justin C. Wedal, William J. Evans, et al.

DECEMBER 28, 2022

INORGANIC CHEMISTRY

READ 🗹

$\label{eq:Gold(I)} \textbf{Gold(I)} \cdots \textbf{Lanthanide(III) Bonds in Discrete Heterobimetallic } \\ \textbf{Compounds: A Combined Computational and Topological } \\ \textbf{Study}$

Daniel Blasco and Dage Sundholm

DECEMBER 07, 2022

INORGANIC CHEMISTRY

READ **C**

dl-Alanine Covalently Bonded Giant Arsenotungstate with Rapid Photochromic and Decent Proton Conduction Properties

Kangting Zheng, Jingyang Niu, et al.

DECEMBER 08, 2022

INORGANIC CHEMISTRY

READ

Get More Suggestions >